

LhARA: The Laser-hybrid Accelerator for Radiobiological Applications

G. Aymar¹, T. Becker², S. Boogert³, M. Borghesi⁴, R. Bingham^{5,1},
C. Brenner¹, P.N. Burrows⁶, O.C. Ettlinger⁷, T. Dascalu⁸, S. Gibson³,
T. Greenshaw⁹, S. Gruber¹⁰, D. Gujral¹¹, C. Hardiman¹¹, J. Hughes⁹,
W.G. Jones^{8,20}, K. Kirkby¹², A. Kurup⁸, J-B. Lagrange¹, K. Long^{8,1}, W. Luk⁸,
J. Matheson¹, P. McKenna^{5,14}, R. McLauchlan¹¹, Z. Najmudin⁷, H.T. Lau⁸,
J.L. Parsons^{9,21}, J. Pasternak^{8,1}, J. Pozimski^{8,1}, K. Prise⁴, M. Puchalska¹³,
P. Ratoff¹⁴, G. Schettino^{15,19}, W. Shields³, S. Smith¹⁶, J. Thomason¹,
S. Towe¹⁷, P. Weightman⁸, C. Whyte⁵, R. Xiao¹⁸

¹ STFC Rutherford Appleton Laboratory, Harwell Oxford, Didcot, OX11 0QX, UK

² Maxeler Technologies Limited, 3 Hammersmith Grove, London W6 0ND, UK

³ John Adams Institute for Accelerator Science, Royal Holloway, University of London, Egham, Surrey, TW20 0EX, UK

⁴ Queens University Belfast, University Road, Belfast, BT7 1NN, Northern Ireland, UK

⁵ Department of Physics, SUPA, University of Strathclyde, 16 Richmond Street, Glasgow, G1 1XQ, UK

⁶ John Adams Institute for Accelerator Science, University of Oxford, Denys Wilkinson Building, Keble Road, Oxford OX1 3RH, UK

⁷ John Adams Institute for Accelerator Science, Imperial College London, Exhibition Road, London, SW7 2AZ, UK

⁸ Imperial College London, Exhibition Road, London, SW7 2AZ, UK

⁹ University of Liverpool, Liverpool L3 9TA, UK

¹⁰ Christian Doppler Laboratory for Medical Radiation Research for Radiation Oncology, Medical University of Vienna, Spitalgasse 23, 1090 Vienna, Austria

¹¹ Imperial College NHS Healthcare Trust, The Bays, South Wharf Road, St Mary's Hospital, London W2 1NY, UK

¹² University of Manchester, Oxford Road, Manchester, M13 9PL, UK

¹³ Technische Universität Wien, Atominstitut, Stadionallee 2, 1020 Vienna, Austria

¹⁴ Cockcroft Institute, Daresbury Laboratory, Sci-Tech Daresbury, Daresbury, Warrington, WA4 4AD, UK

¹⁵ National Physical Laboratory, Hampton Road, Teddington, Middlesex, TW11 0LW, UK

¹⁶ STFC Daresbury Laboratory, Daresbury, Cheshire, WA4 4AD, UK

¹⁷ Leo Cancer Care, Broadview, Windmill Hill, Hailsham, East Sussex, BN27 4RY, UK

¹⁸ Corerain Technologies, 14F, Changfu Jinmao Building (CFC), Trade-free Zone, Futian District, Shenzhen, Guangdong, China

¹⁹ University of Surrey, 388 Stag Hill, Guilford, GU2 7XH, UK

²⁰ Imperial Patient and Public Involvement Group (IPPIG), Imperial College London, Exhibition Road, London, SW7 2AZ, UK

²¹ The Clatterbridge Cancer Centre, Bebington, CH63 4JY, UK

This is a provisional file, not the final typeset article

Correspondence*: A. Kurup
a.kurup@imperial.ac.uk

2 ABSTRACT

3 The ‘Laser-hybrid Accelerator for Radiobiological Applications’, LhARA, is conceived as a novel,
4 flexible facility dedicated to the study of radiobiology. The technologies demonstrated in LhARA,
5 which have wide application, will be developed to allow particle-beam therapy to be delivered in
6 a new regimen, combining a variety of ion species in a single treatment fraction and exploiting
7 ultra-high dose rates. LhARA will be a hybrid accelerator system in which laser interactions drive
8 the creation of a large flux of protons or light ions that are captured using a plasma (Gabor)
9 lens and formed into a beam. The laser-driven source allows protons and ions to be captured
10 at energies significantly above those that pertain in conventional facilities, thus evading the
11 current space-charge limit on the instantaneous dose rate that can be delivered. The laser-hybrid
12 approach, therefore, will allow the radiobiology that determines the response of tissue to ionising
13 radiation to be studied with protons and light ions using a wide variety of time structures, spectral
14 distributions, and spatial configurations at instantaneous dose rates up to and significantly beyond
15 the ultra-high dose-rate ‘FLASH’ regime.

16 It is proposed that LhARA be developed in two stages. In the first stage, a programme of *in*
17 *vitro* radiobiology will be served with proton beams with energies between 10 MeV and 15 MeV.
18 In stage two, the beam will be accelerated using a fixed-field accelerator (FFA). This will allow
19 experiments to be carried out *in vitro* and *in vivo* with proton beam energies of up to 127 MeV.
20 In addition, ion beams with energies up to 33.4 MeV per nucleon will be available for *in vitro*
21 and *in vivo* experiments. This paper presents the conceptual design for LhARA and the R&D
22 programme by which the LhARA consortium seeks to establish the facility.

23 LAY SUMMARY

24 It is well established that radiation therapy (RT) is an effective treatment for many types of cancer.
25 Most treatments are delivered by machines that accelerate electrons which are then used to
26 produce a beam of high-energy photons (X-rays) which are directed at a tumour to kill cancer
27 cells. However, healthy tissue anywhere in the path of the photon beam is also irradiated and so
28 can be damaged. Modern X-ray therapy is able to reduce this damage by using several beams at
29 different angles.

30 Recent years have seen the use of a new type of machine in which protons are accelerated to
31 produce proton beams (rather than photon beams) which are directed at a tumour. These proton
32 beams can be arranged to deposit almost all of their energy in a small volume within a tumour so
33 they cause little damage to healthy tissue; a major advantage over photon beams. But proton
34 machines are large and expensive, so there is a need for the development of proton machines
35 that are smaller, cheaper and more flexible in how they can be used.

36 The LhARA project is aimed at the development of such proton machines using a new approach
37 based on high powered lasers. Such new machines could also make it easier to deliver the dose
38 in very short high-intensity pulses and as a group of micro-beams—exciting recent research has
39 shown that this brings improved effectiveness in killing cancer cells while sparing healthy tissue.
40 The technology to be proved in LhARA should enable a course of RT to be delivered in days
41 rather than weeks.

42 Scientifically, there is a need to understand better the basic processes by which radiation
43 interacts with biological matter to kill cancer cells—the investigation of these processes involves
44 physics as well as biology. Thus the most important aim of LhARA is to pursue this radiobiological

45 research in new regimens and from this to develop better treatments. LhARA will also pursue
46 technological research into laser-hybrid accelerators.

47 **Keywords:** Radiobiology, Novel acceleration, Proton beam therapy, Ion beam therapy, Laser-driven acceleration, Plasma lens, Fixed
48 field alternating gradient acceleration

1 INTRODUCTION

49 Cancer is the second most common cause of death globally [The World Health Organisation (2020)]. In
50 2018, 18.1 million new cancer cases were diagnosed, 9.6 million people died of cancer-related disease, and
51 43.8 million people were living with cancer [Bray et al. (2018); Fitzmaurice et al. (2018)]. It is estimated
52 that 26.9 million life-years could be saved in low- and middle-income countries if radiotherapy capacity
53 could be scaled up [Atun et al. (2015)]. Novel techniques incorporated in facilities that are at once robust,
54 automated, efficient, and cost-effective are required to deliver the required scale-up in provision.

55 Radiation therapy (RT), a cornerstone of cancer treatment, is used in over 50 % of cancer patients [Datta
56 et al. (2019)]. The most frequently used types of radiotherapy employ photon or electron beams with
57 MeV-scale energies. Proton and ion beams offer substantial advantages over X-rays because the bulk of
58 the beam energy is deposited in the Bragg peak. This allows dose to be conformed to the tumour while
59 sparing healthy tissue and organs at risk. The benefits of proton and ion-beam therapy (PBT) are widely
60 recognised. PBT today is routinely delivered in fractions of ~ 2 Gy per day over several weeks; each
61 fraction being delivered at a rate of $\lesssim 5$ Gy/minute deposited uniformly over the target treatment volume.
62 Evidence of therapeutic benefit when dose is delivered at ultra-high rate, $\gtrsim 40$ Gy/s, in “FLASH” RT [Berry
63 (1973); Favaudon et al. (2014); Durante et al. (2018); Voznin et al. (2019); Wilson et al. (2020b)] or
64 when multiple micro-beams with diameter less than 1 mm distributed over a grid with inter-beam spacing
65 ~ 3 mm are used [Prezado and Fois (2013); Prezado et al. (2017b,a, 2018); González and Prezado (2018);
66 Martínez-Rovira et al. (2017)]. However, the radiobiological mechanisms by which the therapeutic benefit
67 is generated using these approaches are not entirely understood.

68 LhARA, the Laser-hybrid Accelerator for Radiobiological Applications, is conceived as the new, highly
69 flexible, source of radiation that is required to explore the mechanisms by which the biological response to
70 ionising radiation is determined by the physical characteristics of the beam. A high-power pulsed laser will
71 be used to drive the creation of a large flux of protons or light ions which are captured and formed into a
72 beam by strong-focusing plasma lenses. The plasma (Gabor) lenses provide the same focusing strength
73 as high-field solenoids at a fraction of the cost. Rapid acceleration will be performed using a fixed-field
74 alternating-gradient accelerator (FFA) thereby preserving the unique flexibility in the time, energy, and
75 spatial structure of the beam afforded by the laser-driven source.

76 The LhARA facility may be developed in two stages. In the first stage, the laser-driven beam, captured
77 and transported using plasma lenses and bending magnets, will serve a programme of *in vitro* radiobiology
78 with proton beams of energy of up to 15 MeV. In stage two, the beam will be accelerated using an FFA. This
79 will allow experiments to be carried out *in vitro* and *in vivo* with proton-beam energies of up to 127 MeV.
80 Ion beams (including C⁶⁺) with energies up to 33.4 MeV per nucleon will also be available.

81 The laser pulse that initiates the production of protons or ions at LhARA may be triggered at a repetition
82 rate of up to 10 Hz. The time structure of the beam may therefore be varied to interrupt the chemical
83 and biological pathways that determine the biological response to ionising radiation with 10 ns to 40 ns
84 long proton or ion bunches repeated at intervals as small as 100 ms. The technologies chosen to capture,
85 transport, and accelerate the beam in LhARA ensure that this unique capability is preserved. The LhARA
86 beam may be used to deliver an almost uniform dose distribution over a circular area with a maximum
87 diameter of between 1 cm and 3 cm. Alternatively, the beam can be focused to a spot with diameter of
88 ~ 1 mm.

89 The technologies demonstrated in LhARA have the potential to be developed to make particle-beam
90 therapy (PBT) available to the many. The laser-hybrid approach will allow radiobiological studies and

91 eventually radiotherapy to be carried out in completely new regimens, delivering a variety of ion species in
92 a broad range of time structures, spectral distributions, and spatial configurations at instantaneous dose
93 rates up to and potentially significantly beyond the current ultra-high dose-rate “FLASH” regime.

94 The “pre Conceptual Design Report” (pre-CDR) for LhARA [The LhARA consortium (2020)] lays the
95 foundations for the development of full conceptual and technical designs for the facility. The pre-CDR also
96 contains a description of the R&D that is required to demonstrate the feasibility of critical components
97 and systems. This paper presents a summary of the contents of the pre-CDR and lays out the vision of the
98 consortium.

99

2 MOTIVATION

100 RT delivered using protons and ions, particle-beam therapy (PBT), has the potential to overcome some
101 of the fundamental limitations of X-rays in cancer treatment through targeted delivery of the radiation
102 dose [Loeffler and Durante (2013)]. The Particle Therapy Co-Operative Group (PTCOG) currently lists
103 90 proton therapy facilities and 12 carbon ion therapy facilities, located predominantly in high-income
104 countries [PTCOG (2020)]. Low- and middle-income countries (LMIC) are relatively poorly served, indeed
105 nearly 70% of cancer patients globally do not have access to RT [Datta et al. (2019)].

106 The case for a systematic study of the radiobiology of proton and ion beams

107 The efficacy of proton and ion beams is characterised by their relative biological effectiveness (RBE) in
108 comparison to a reference photon beam. The treatment-planning software that is in use in the clinic today
109 assumes an RBE value for protons of 1.1 [Paganetti and van Luijk (2013)], meaning that, compared to
110 X-rays, a lower dose of protons is needed to produce the same therapeutic effect. However, the rapid
111 rise in the linear energy transfer (LET) at the Bragg peak leads to significant uncertainties in the RBE.
112 Furthermore, it is known that RBE depends strongly on many factors, including particle energy, dose, dose
113 rate, the degree of hypoxia, and tissue type [Paganetti (2014)]. Indeed, RBE values from 1.1 to over 3
114 have been derived from *in vitro* clonogenic-survival assay data following proton irradiation of cultured
115 cell lines derived from different tumours [Paganetti (2014); Chaudhary et al. (2014); Wilkens and Oelfke
116 (2004)]. RBE values of ~ 3 are accepted for high-LET carbon-ion irradiation, although higher values have
117 been reported [Karger and Peschke (2017)]. RBE uncertainties for carbon and other ion species are at
118 least as large as they are for protons. These uncertainties can lead to an incorrect estimation of the dose
119 required to treat a particular tumour. Overestimation can lead to risk of damage to healthy tissue, while an
120 underestimate can lead to the tumour not being treated sufficiently for it to be eradicated.

121 The radio-therapeutic effect is caused largely by irreparable damage to the cell’s DNA. The spectrum of
122 DNA damage induced within tumour cells changes in response to differences in RBE. Larger RBE values,
123 corresponding to higher LET, can increase the frequency and complexity of DNA damage, particularly
124 DNA double-strand breaks (DSB) and complex DNA damage (CDD) where multiple DNA lesions are
125 induced in close proximity [Vitti and Parsons (2019); Carter et al. (2018)]. These DNA lesions are a major
126 contributor to radiation-induced cell death as they represent a significant barrier to the cellular DNA-repair
127 machinery [Vitti and Parsons (2019)]. However, a number of other biological factors contribute to varying
128 RBE in specific tumours, including the intrinsic radio-sensitivity of the tissue, the level of oxygenation
129 (hypoxia), the growth and re-population characteristics, and the associated tumour micro-environment.
130 Consequently there is still significant uncertainty in the precise radiobiological mechanisms that arise and
131 how these mechanisms are affected by PBT. Detailed systematic studies of the biophysical effects of the
132 interaction of protons and ions, under different physical conditions, with different tissue types will provide

133 important information on RBE variation and could enable enhanced patient treatment-planning algorithms
134 to be devised. In addition, studies examining the impact of combination therapies with PBT (e.g. targeting
135 the DNA damage response, hypoxia signalling mechanisms and also the tumour micro-environment) are
136 currently sparse; performing these studies will therefore provide input vital to the development of future
137 personalised patient-therapy strategies using PBT.

138 **The case for novel beams for radiobiology**

139 PBT delivery to date has been restricted to a small range of beam characteristics. Significantly reduced
140 lung fibrosis in mice, skin toxicity in mini-pigs, and reduced side-effects in cats with nasal squamous-cell
141 carcinoma have been observed which is currently thought to be mediated via local oxygen depletion [Wilson
142 et al. (2020b,a)]. In fact, the first patient with CD30+ T-cell cutaneous lymphoma has been safely treated
143 with electrons delivered at FLASH dose rates [Bourhis et al. (2019)]. In addition, therapeutic benefit has
144 been demonstrated with the use of multiple micro-beams [Prezado et al. (2017b)]. However, there is still
145 significant uncertainty regarding the thresholds and the radiobiological mechanisms by which therapeutic
146 benefit is generated in FLASH and micro-beam therapy. Extensive further study both *in vitro* and in
147 appropriate *in vivo* models is required.

148 The LhARA facility will provide access to stable ion beams, provide a wide variety of temporal,
149 spatial, and spectral fractionation schemes, and deliver reliable and reproducible biological data with
150 fewer constraints than at current clinical centres. The availability of several ion beams (from protons to
151 heavier ions) within the same facility will provide further flexibility, and the ability to perform direct
152 radiobiological comparisons of the effects of different charged particles at different energies and dose
153 rates, and to perform mechanistic studies (e.g. examining the oxygen depletion hypothesis for FLASH)
154 will be unique. In addition, LhARA will enable exhaustive evaluations of RBE using more complex
155 end-points (e.g. angiogenesis and inflammation) in addition to routine survival measurements. The ability
156 to evaluate charged particles in conjunction with other therapies (immunotherapy and chemotherapy), and
157 of performing *in vivo* experiments with the appropriate animal models is a huge advantage given the current
158 lack of evidence in these areas. LhARA therefore has the potential to provide the radiobiological data
159 required to improve clinical practice. The simulations of LhARA that are described in this document have
160 been used to estimate the dose delivered as a function of energy for protons and carbon ions. Details of the
161 simulations can be found in sections 3.3 and 3.4. The simulations show instantaneous particle rates of the
162 order of 10^9 particles per shot can be achieved, corresponding to average dose rates of up to $\gtrsim 120$ Gy/s
163 for protons and $\gtrsim 700$ Gy/s for carbon ions. These estimates are based on the baseline specifications for
164 LhARA.

165 **Laser-hybrid beams for radiobiology and clinical application**

166 High-power lasers have been proposed as an alternative to conventional proton and carbon-ion facilities for
167 radiotherapy [Bulanov et al. (2002); Fourkal et al. (2003); Malka et al. (2004)]. Laser-driven sources have
168 also been proposed to serve as the basis of electron, proton and ion-beams for radiobiology [Kraft et al.
169 (2010); Fiorini et al. (2011); Yogo et al. (2011); Bin et al. (2012); Doria et al. (2012); Zeil et al. (2013);
170 Masood et al. (2014); Zlobinskaya et al. (2014)]. While a number of cell irradiation experiments have been
171 conducted with laser-accelerated ions [Doria et al. (2012); Zeil et al. (2013); Pommarel et al. (2017); Manti
172 et al. (2017)], these have been limited in scope to a single-shot configuration. More recent projects (e.g.
173 A-SAIL [A-SAIL Project (2020)], ELI [Cirrone et al. (2013)] and SCAPA [Wiggins et al. (2019)]) will also
174 investigate radiobiological effects using laser-driven ion beams. These studies will also address various
175 technological issues [Manti et al. (2017); Romano et al. (2016a); Masood et al. (2017); Chaudhary et al.
176 (2017); Margarone et al. (2018)].

177 A beam line to provide ion-driven beams for multi-disciplinary applications, ELIMAIA (ELI
178 Multidisciplinary Applications of laser-Ion Acceleration) is being brought into operation at the Extreme
179 Light Infrastructure (ELI) [Cirrone et al. (2020); Schillaci et al. (2019)]. This beam line will include the
180 “ELI MEDical and multidisciplinary applications” (ELIMED) beam line which will allow radiobiological
181 investigations to be carried out [Cirrone et al. (2016); Romano et al. (2016b); Milluzzo et al. (2017); Pipek
182 et al. (2017); Milluzzo et al. (2018); Cirrone et al. (2020)]. LhARA is distinguished from this facility in
183 that the energy at which the beam will be captured has been chosen to maximise the shot-to-shot stability
184 of the particle flux.

185 Protons and ions at conventional facilities are captured at energies of several tens of keV. At such low
186 energies the mutual repulsion of the particles, the “space-charge effect”, limits the maximum instantaneous
187 dose rate. The laser-driven source allows protons and ions to be captured at energies significantly above
188 those that pertain in conventional facilities, thus evading the current space-charge limit. Rapid acceleration
189 will be performed using a fixed-field alternating-gradient accelerator (FFA) thereby preserving the unique
190 flexibility in the time, energy, and spatial structure of the beam afforded by the laser-driven source. Modern
191 lasers are capable of delivering a Joule of energy in pulses that are tens of femtoseconds in length at
192 repetition rates of $\gtrsim 10$ Hz. Laser-driven ion sources create beams that are highly divergent, have a large
193 energy spread, and an intensity that can vary by up to 25% pulse-to-pulse [Dover et al. (2020)]. These
194 issues are addressed in the conceptual design through the use of Gabor lenses to provide strong focusing
195 and to allow energy selection. In addition, sophisticated instrumentation will be used in a fast feedback-
196 and-control system to ensure that the dose delivered is both accurate and reproducible. This approach will
197 allow multiple ion species, from proton to carbon, to be produced from a single laser by varying the target
198 foil and particle-capture optics.

199 LhARA will prove the principle of the novel technologies required for the development of future therapy
200 facilities. The legacy of the LhARA programme will therefore be: a unique facility dedicated to the
201 development of a deep understanding of the radiobiology of proton and ion beams; and the demonstration
202 in operation of technologies that will allow PBT to be delivered in completely new regimes.
203

3 THE LHARA FACILITY

204 The LhARA facility, shown schematically in figure 1, has been designed to serve two end stations for
205 *in vitro* radiobiology and one end station for *in vivo* studies. The principle components of the LhARA
206 accelerator are: the laser-driven proton and ion source; the matching and energy selection section; beam
207 delivery to the low-energy *in vitro* end station; the low-energy abort line; the injection line for the fixed-
208 field alternating-gradient accelerator (FFA); the FFA; the extraction line; the high-energy abort line; beam
209 delivery to the high-energy *in vitro* end station; and the transfer line to the *in vivo* end station. Proton beams
210 with energies of between 12 MeV and 15 MeV will be delivered directly from the laser-driven source to
211 the low-energy *in vitro* end station via a transfer line. The high-energy *in vitro* end station and the *in vivo*
212 end station will be served by proton beams with energy between 15 MeV and 127 MeV and by ion beams,
213 including C⁶⁺ with energies up to 33.4 MeV/u. The design parameters for the various components of
214 LhARA are given in tables 1 and 2. The design of the LhARA facility is described in the sections that follow.
215

216 3.1 Laser-driven proton and ion source

217 A novel solution for ion-acceleration is to use a compact, flexible laser-driven source coupled to a state-
218 of-the-art beam-transport line. This allows an accelerating gradient of $\gtrsim 10$ GV/m to be exploited at the

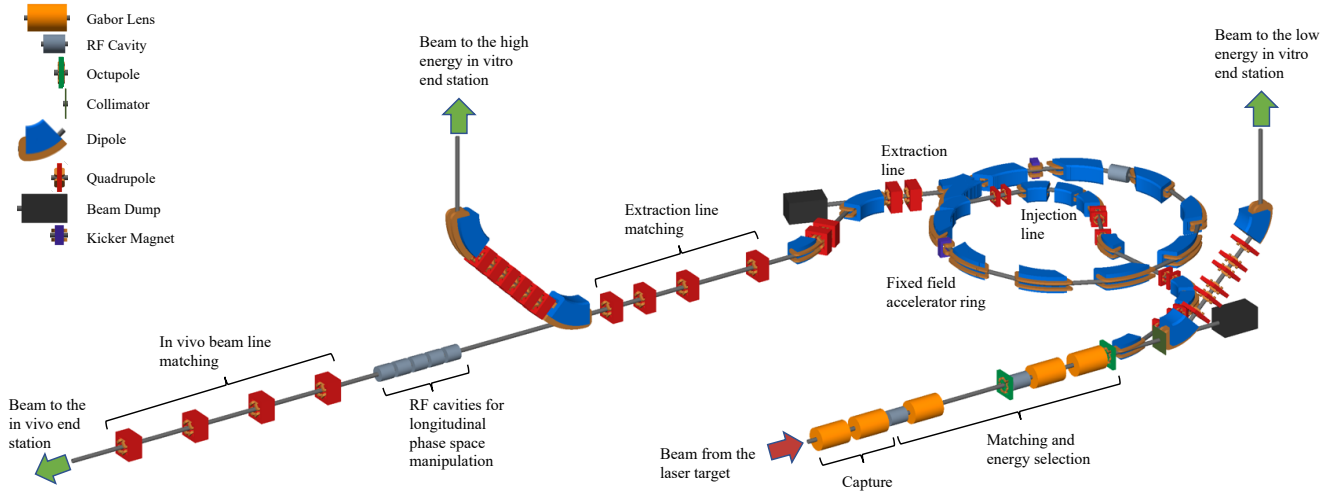


Figure 1. Schematic diagram of the LhARA beam lines. The particle flux from the laser-driven source is shown by the red arrow. Following the ‘Capture’ section is followed by the ‘Matching and energy selection’ sections, the beam is directed either into the 90° bend that takes it to the low-energy *in vitro* end station, towards the FFA injection line, or to the low-energy beam dump. Post acceleration is performed using the FFA on extraction from which the beam is directed either to the high-energy *in vitro* end station, the *in vivo* end station, or the high-energy beam dump. Gabor lenses are shown as orange cylinders, RF cavities as grey cylinders, octopole magnets as green discs, collimators as dark-green bars, dipole magnets are shown in blue, quadrupole magnets are shown in red, beam dumps (black rectangles) and kicker magnets are also shown.

219 laser-driven source. We propose to operate in a laser-driven sheath-acceleration regime [Clark et al. (2000a);
 220 Snavely et al. (2000); Daido et al. (2012)] for ion generation. An intense, short laser pulse will be focused
 221 onto a target. The intense electric field generated on the front surface of the target accelerates the surface
 222 electrons, driving them into the material. Electrons which gain sufficient energy traverse the target, ionising
 223 the material as they go. A strong space-charge electric field, the ‘sheath’, is created as the accelerated
 224 electrons exit the rear surface of the target. This field in turn accelerates surface-contaminant ions. The
 225 sheath-acceleration scheme has been shown to produce ion energies greater than 40 MeV/u at the highest
 226 laser intensities. The maximum proton energy (E_p) scales with laser intensity (I) as, $E_p \propto I^{\frac{1}{2}}$. The laser
 227 required to deliver a significant proton flux at 15 MeV is commercially available.

228 The distribution of proton and ion energies observed in laser-driven beams exhibits a sharp cut off at
 229 the maximum energy and, historically, the flux of laser-accelerated ion beams has varied significantly
 230 shot-to-shot. To reduce the impact of the shot-to-shot variations, the choice has been made to select particles
 231 from the plateau of the two-temperature energy spectrum of the laser-accelerated ion beam [Clark et al.
 232 (2000b); Passoni et al. (2010)]. This choice should enhance ion-beam stability and allow reproducible
 233 measurements to be carried out at ultra-high dose rates using a small number of fractions. To create the flux
 234 required in the plateau region it is proposed that a 100 TW laser system is used. A number of commercial
 235 lasers are available that are capable of delivering $> 2.5\text{ J}$ in pulses of duration $< 25\text{ fs}$, at 10 Hz with
 236 contrast better than $10^{10} : 1$. Shot-to-shot stability of $< 1\%$ is promised, an important feature for stable
 237 ion-beam production.

238 Target

239 Key to the operation of this configuration is a system that refreshes the target material at high-repetition

Table 1. Design parameters of the components of the LhARA facility. The parameter table is provided in a number of sections. This section contains parameters for the Laser-driven proton and ion source, the Proton and ion capture section, and the Stage 1 beam transport section.

Parameter	Value or range	Unit
Laser driven proton and ion source		
Laser power	100	TW
Laser Energy	2.5	J
Laser pulse length	25	fs
Laser rep. rate	10	Hz
Required maximum proton energy	15	MeV
Proton and ion capture		
Beam divergence to be captured	50	mrad
Gabor lens effective length	0.857	m
Gabor lens length (end-flange to end-flange)	1.157	m
Gabor lens cathode radius	0.0365	m
Gabor lens maximum voltage	65	kV
Number of Gabor lenses	2	
Alternative technology: solenoid length	1.157	m
Alternative technology: solenoid max field strength	1.3	T
Stage 1 beam transport: matching & energy selection, beam delivery to low-energy end station		
Number of Gabor lenses	3	
Number of re-bunching cavities	2	
Number of collimators for energy selection	1	
Arc bending angle	90	Degrees
Number of bending magnets	2	
Number of quadrupoles in the arc	6	
Alternative technology: solenoid length	1.157	m
Alternative technology: solenoid max field strength (to serve the injection line to the Stage 2)	0.8 (1.4)	T

240 rate in a reproducible manner. A number of schemes have been proposed for such studies, from high-
 241 pressure gases [Willingale et al. (2009); Bin et al. (2015); Chen et al. (2017)], cryogenic hydrogen ribbons
 242 [Margarone et al. (2016); Gauthier et al. (2017); Obst et al. (2017)], liquid sheets [Morrison et al. (2018)]
 243 and tape drives [Noaman-ul Haq et al. (2017)]. For the LhARA facility, a tape drive based on the system
 244 developed at Imperial College London is proposed. This system is capable of reliable operation at target
 245 thicknesses down to $5\text{ }\mu\text{m}$, using both aluminium and steel foils, and down to $18\text{ }\mu\text{m}$ using plastic tapes.
 246 Such tape-drive targets allow operation at high charge (up to 100 pC at $15 \pm 1\text{ MeV}$, i.e. $> 10^9$ protons per
 247 shot) and of delivering high-quality proton and ion fluxes at repetition rates of up to 10 Hz or greater.

248 The careful control of the tension on the tape in a tape-drive target is critical for reproducible operation.
 249 The tape must be stretched to flatten the surface, without stretching it to its plastic response. Surface
 250 flatness is important for a number of reasons. Rippling of the front surface modifies the laser absorption
 251 dramatically; uncharacterised rippling can make shot-to-shot variations significant and unpredictable
 252 [Noaman-ul Haq et al. (2017)]. Similarly, rear surface perturbations can modify the sheath field, resulting
 253 in spatial non-uniformities of the proton beam or suppression of the achievable peak energies. Tape drives
 254 with torsion control and monitoring to maintain a high-quality tape surface have been designed and operated
 255 in experiments at Imperial College London. The development of these targets continues with a view to the
 256 production of new, thinner tapes for improved ion generation and the creation of ion species other than

Table 2. Design parameters of the components of the LhARA facility. The parameter table is provided in a number of sections. This section contains parameters for the Stage 2 beam transport and the *in vitro* and *in vivo* end stations.

Parameter	Value or range	Unit
Stage 2 beam transport: FFA, transfer line, Number of bending magnets in the injection line	beam delivery to high-energy end stations 7	
Number of quadrupoles in the injection line	10	
FFA: Machine type	single spiral scaling FFA	
FFA: Extraction energy	15–127	MeV
FFA: Number of cells	10	
FFA: Orbit R _{min}	2.92	m
FFA: Orbit R _{max}	3.48	m
FFA: Orbit excursion	0.56	m
FFA: External R	4	m
FFA: Number of RF cavities	2	
FFA: RF frequency	1.46–6.48	MHz
FFA: harmonic number	1, 2 or 4	
FFA: RF voltage (for 2 cavities)	4	kV
FFA: spiral angle	48.7	Degrees
FFA: Max B field	1.4	T
FFA: k	5.33	
FFA: Magnet packing factor	0.34	
FFA: Magnet opening angle	12.24	degrees
FFA: Magnet gap	0.047	m
FFA: Ring tune (x,y)	(2.83,1.22)	
FFA: γ_T	2.516	
FFA: Number of kickers	2	
FFA: Number of septa	2	
Number of bending magnets in the extraction line	2	
Number of quadrupoles in the extraction line	8	
Vertical arc bending angle	90	Degrees
Number of bending magnets in the vertical arc	2	
Number of quadrupoles in the vertical arc	6	
Number of cavities for longitudinal phase space manipulation	5	
Number of quadrupoles in the in vivo beam line	4	
<i>In vitro</i> biological end stations		
Maximum input beam diameter	1-3	cm
Beam energy spread (full width)	Low-energy end station: ≤ 4 High-energy end station: ≤ 1	%
Input beam uniformity	< 5	%
Scintillating fibre layer thickness	0.25	mm
Air gap length	5	mm
Cell culture plate thickness	1.3	mm
Cell layer thickness	0.03	mm
Number of end stations	2	
<i>In vivo</i> biological end station		
Maximum input beam diameter	1-3	cm
Beam energy spread (full width)	≤ 1	%
Input beam uniformity	< 5	%
Beam options	Spot-scanning, passive scattering, micro-beam	

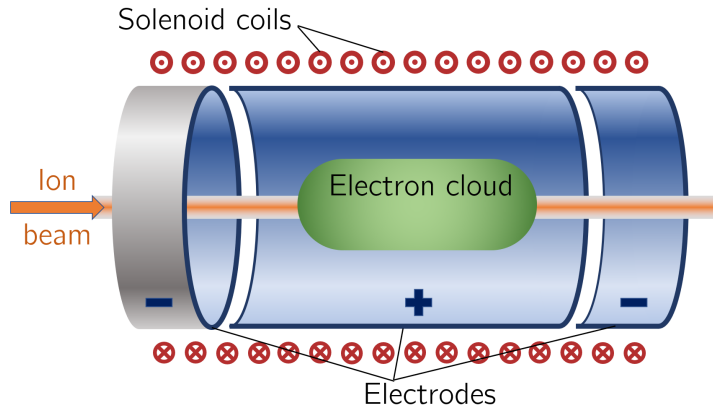


Figure 2. Schematic diagram of a Penning-Malmberg trap of the type proposed for use in the Gabor lenses to be used in LhARA. The solenoid coils, and the direction of current flow, are indicated by the red circles. The confining electrostatic potential is provided using a central cylindrical anode and two cylindrical negative end electrodes. The ion beam enters on-axis from the left and the electron cloud is indicated by the green shaded area.

257 proton and carbon. This is an active area of R&D that will continue with the development of LhARA.

258
259

3.2 Proton and ion capture

260 The use of an electron cloud as a focusing element for charged-particle beams was first proposed by
261 Gabor [Gabor (1947)]. The electron could is confined within the lens using a long cylindrical anode placed
262 within a uniform solenoid field, see figure 2. Such a configuration is commonly known as a ‘Penning
263 trap’ and has found wide application in many fields [Thompson (2015)]. Variations on the Penning trap
264 where axial apertures in the cathodes are introduced, such as the Penning-Malmberg trap [deGrassie and
265 Malmberg (1980); Malmberg et al. (1988)] are attractive for beam-based applications due to the excellent
266 access provided to the plasma column.

267 The focal length of a Gabor lens of length l is given in terms of the electron number density by:

$$\frac{1}{f} = \frac{e^2 n_e}{4\epsilon_0 U} l; \quad (1)$$

268 where e is the magnitude of the electric charge of the electron, n_e is the number density of the electrons
269 confined within the lens, ϵ_0 the permittivity of free space, and U is the kinetic energy of the particle beam.
270 The desired focussing strength determines n_e which in turn allows the anode voltage and magnetic-field
271 strength to be determined [Reiser (1989); Pozimski and Aslaninejad (2013)]. The focal length of the Gabor
272 lens is inversely proportional to the number density of electrons trapped in the cloud. The focal lengths
273 desired to capture the proton and ion beams at LhARA have been chosen such that the required electron
274 number densities are conservative and lie within the range achieved in published experiments.

275 For a given focal length, the magnetic field required in the Gabor lens is reduced compared to that of a
276 solenoid that would give equivalent focusing. In the non-relativistic approximation the relationship between
277 the magnetic field in the Gabor lens, B_{GBL} , and the equivalent solenoid, B_{sol} , is given by [Pozimski and

278 Aslaninejad (2013)]:

$$B_{\text{GPL}} = B_{\text{sol}} \sqrt{Z \frac{m_e}{m_p}}; \quad (2)$$

279 where Z is the charge state of the ions. In the case of a proton beam the reduction factor is 43. This means
280 the cost of the solenoid for a Gabor lens can be significantly lower than the cost for a solenoid of equivalent
281 focusing strength.

282 Instability of the electron cloud is a concern in the experimental operation of a Gabor lens; azimuthal
283 beam disruption due to the diocotron instability has been observed and described theoretically [Meusel et al.
284 (2013)]. Theory indicates that the diocotron instability is most problematic under well-defined geometric
285 conditions. The reliable operation of a Gabor lens in a regime free from this instability has yet to be
286 demonstrated. Gabor lenses promise very strong focusing, simple construction, and low magnetic field,
287 all attractive features for LhARA. However, these attractive features come at the cost of relatively high
288 voltage operation ($\gtrsim 50$ kV) and possible vulnerability to instability.

289 With reliable operation of Gabor lenses as yet unproven, we plan a two-part experimental and theoretical
290 programme of research to prove Gabor-lens suitability. Initial work will include: theoretical investigation
291 of lens stability in a full 3D particle-in-cell code such as VSIM [VSI (2020)]; and the development of
292 electron-density diagnostics based on interferometric measurement of the refractive-index change. A test
293 Gabor lens will be constructed to allow validation of both the simulation results and a new diagnostic using
294 an alpha emitter as a proxy for the LhARA beam. In addition, the initial investigation will include the
295 design of an electron beam to fill the lens. Should it prove not to be possible to produce a suitable Gabor
296 lens it will be necessary to use high-field solenoids to produce the equivalent focusing effect.

297

298 **3.3 Beam transport and delivery to the low-energy *in vitro* end station**

299 Beam-transport to the low-energy *in vitro* end station is required to deliver a uniform dose distribution at
300 the cell layer. Beam losses must be minimised for radiation safety and to maximise the dose that can be
301 delivered in a single shot. The transport line has been designed to minimise regions in which the beam
302 is brought to a focus to reduce the impact of space-charge forces on the beam phase-space. An optical
303 solution was initially developed using Beamoptics [Autin et al. (1998)] and MADX [Grote and Schmidt
304 (2003)]. Accurate estimation of the performance of the beam line requires the inclusion of space-charge
305 forces and particle-matter interactions. Therefore, performance estimation was performed using Monte
306 Carlo particle-tracking from the ion source to the end station. BDSIM [Nevay et al. (2020)], which is based
307 on the Geant4 toolkit was used for the simulation of energy deposition arising from beam interactions with
308 the material in the accelerator and the end station. GPT [De Loos and Van der Geer (1996)] was used for
309 evaluating the full 3D impact of space-charge.

310 An idealised Gaussian beam was generated with a spot size of $4 \mu\text{m}$ FWHM, an angular divergence of
311 50 mrad , 35 fs FWHM bunch length, and an energy spread of $1 \times 10^{-6} \text{ MeV}$. The maximum estimated
312 bunch charge is 1×10^9 protons. The presence of a substantial electron flux produced from the laser target
313 compensates the high proton charge density in the vicinity of the ion-production point. To approximate the
314 partial space-charge compensation in the vicinity of the target it was assumed that co-propagating electrons
315 would fully compensate the space-charge forces over the first 5 cm of beam propagation. Beyond this, the
316 proton beam was assumed to have separated from the co-propagating electrons sufficiently for space-charge
317 to become a prominent effect and cause emittance growth. Therefore, a further 5 cm drift was simulated
318 including space-charge forces. At a distance of 10 cm from the ion source the beam is at the exit of the

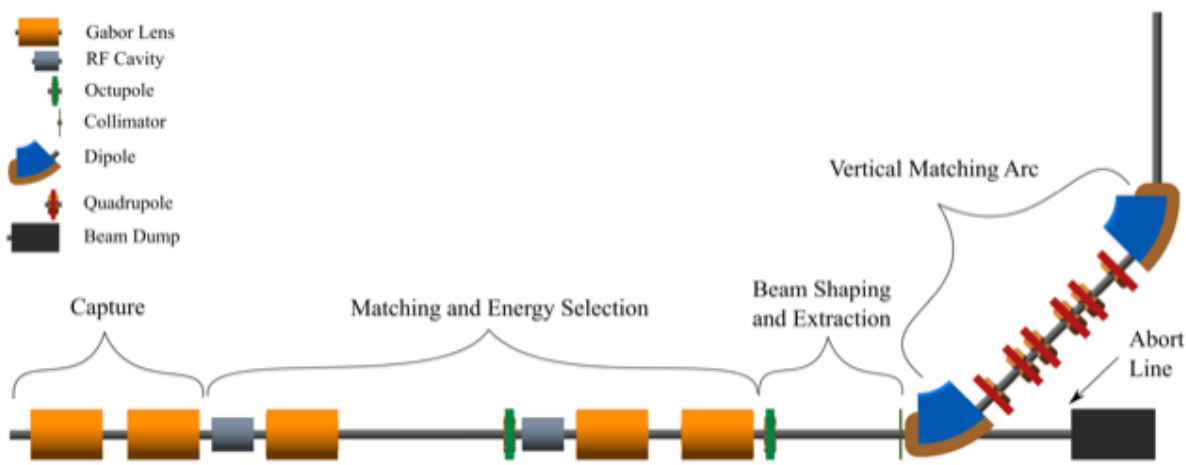


Figure 3. Beam transport for Stage 1 of LhARA visualised in BDSIM, showing five machine sections. The capture section is composed of two Gabor lenses (orange cylinders). The matching and energy selection section includes three Gabor lenses, two RF cavities (grey cylinders) and an octupole magnet (green disc). The beam shaping and extraction section includes a second octupole and a collimator (vertical dark-green bar). The vertical matching arc directs the beam into the low-energy *in vitro* end station and is composed of two 45° dipoles (blue and brown) and six quadrupoles (red). The total length of this beam line is 17.3 m.

319 laser-target vessel. The kinematic distributions of ions in the beam were stored at this point and passed to
320 the relevant BDSIM and GPT simulations of the downstream beam line.

321 The beam line, shown schematically in figure 3, is composed of five sections: beam capture; matching
322 and energy selection; beam shaping; vertical arc matching; and an abort line. The capture section uses two
323 Gabor lenses to minimise the transverse momentum of particles in the beam. Beyond the capture section,
324 an RF cavity permits control of the bunch length and manipulation of the longitudinal phase-space. A third
325 Gabor lens then focuses the bunch to a small spot size after which a second RF cavity is located to provide
326 further longitudinal phase-space manipulation. Two further Gabor lenses bring the beam parallel once more
327 in preparation for the vertical 90° arc. All Gabor lenses have an inner radius of 3.65 cm and an effective
328 length of 0.857 m. All lenses operate at a cathode voltage of less than 65 kV.

329 A parallel beam emerges from the final Gabor lens, providing significant flexibility for the inclusion
330 of beam shaping and extraction systems. Beam uniformity will be achieved using octupole magnets to
331 provide third-order focusing to perturb the first-order focusing from the Gabor lenses. Such schemes have
332 been demonstrated in magnetic lattices in a number of facilities [Tsoupas et al. (1991); Urakabe et al.
333 (1999); Amin et al. (2018)]. A suitable position for the first octupole was identified to be after the final
334 Gabor lens where the beam is large; its effect on the beam is expected to be significant. Octupoles were
335 only modelled in BDSIM as GPT does not have a standard component with an octupolar field. The typical
336 rectangular transverse distribution resulting from octupolar focusing requires collimation to match the
337 circular aperture through which the beam enters the end station. A collimator is therefore positioned at the
338 start of the vertical arc. Further simulations are required to determine the optimum position of the second
339 octupole and to evaluate the performance of the octupoles. The switching dipole which directs the beam to
340 the injection line of the FFA in Stage 2 will be located between the second octupole and the collimator,
341 requiring the octupole to be ramped down for Stage 2 operation.

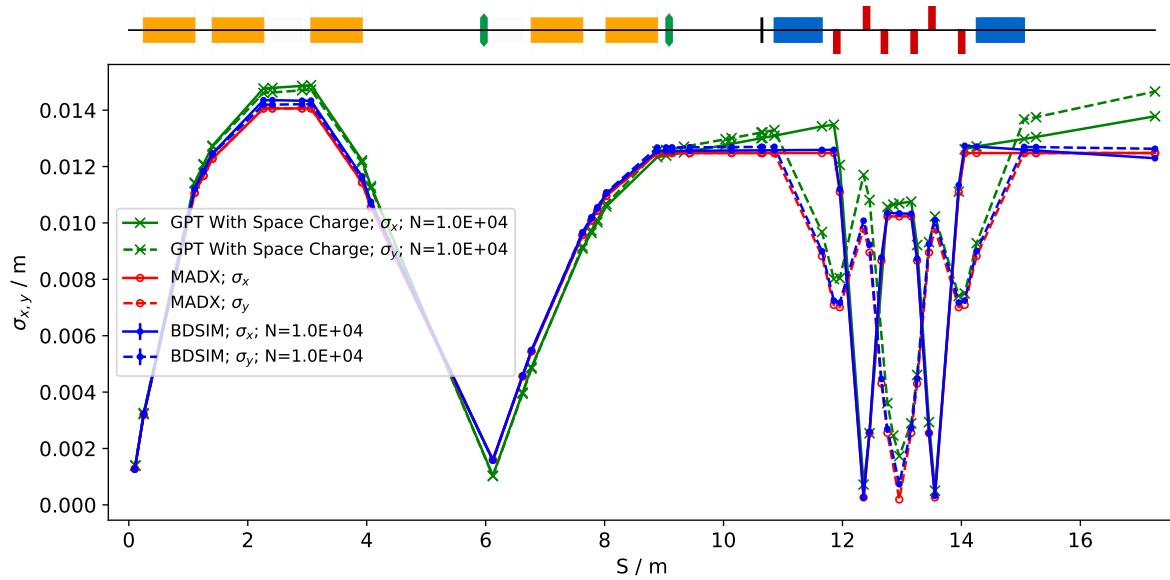


Figure 4. Horizontal (solid lines) and vertical (dashed lines) beam sizes through the *in vitro* beam transport, simulated with space-charge in GPT (green), and without space-charge in MADX (red) and BDSIM (blue).

342 The vertical arc uses transparent optics in an achromat matching section to ensure that the first-order
 343 transfer map through the arc is equivalent to the identity transformation and that any dispersive effects are
 344 cancelled. A 2 m drift tube is added after the arc to penetrate the concrete shielding of the end station floor
 345 and to bring the beam to bench height. The abort line consists of a drift followed by a beam dump and
 346 requires the first vertical dipole to ramp down, preventing charged-particle transportation to the end station.

347 The underlying physics of plasma-lens operation cannot be simulated in BDSIM or GPT, however it
 348 can be approximated using solenoid magnets of equivalent strength. RF cavity fields were not simulated.
 349 10 000 particles were simulated corresponding to the estimated maximum bunch charge of 1×10^9 protons.
 350 Figure 4 shows excellent agreement between horizontal and vertical transverse beam sizes in BDSIM
 351 and MADX, verifying the beam line's performance in the absence of space-charge effects. Reasonable
 352 agreement between BDSIM and GPT is also seen when space-charge forces are included in GPT. Emittance
 353 growth is observed prior to the first solenoid, affecting the optical parameters throughout the machine.
 354 However, the resulting beam dimensions at the cell layer of 1.38 cm horizontally and 1.47 cm vertically
 355 are not significantly different from the ideal beam in BDSIM. Further adjustments of the Gabor lenses
 356 and arc-quadrupole strengths may compensate for this. The transmission efficiency of the beam line is
 357 approximately 100%.

358 The small bunch dimensions in both transverse planes at the focus after the third Gabor lens, where
 359 the energy selection collimator will be placed, remain a concern if the effect of space-charge has been
 360 underestimated. Similar bunch dimensions are achieved in the vertical arc, however, quadrupolar focusing
 361 is confined to a single plane mitigating further emittance growth.

362 To investigate beam uniformity, BDSIM simulations with and without octupoles and collimation for
 363 beam shaping were conducted. Each octopole was assumed to have a magnetic length of 0.1 m and pole-tip
 364 radius of 5 cm. The strength parameter, k_3 , of each octopole was arbitrarily set to 6000. A 2 cm thick iron
 365 collimator with a 40 mm diameter aperture was positioned 1.5 m downstream of the octopole. Figure 5
 366 shows the beam phase-space and particle distributions at the end station for the transverse and longitudinal

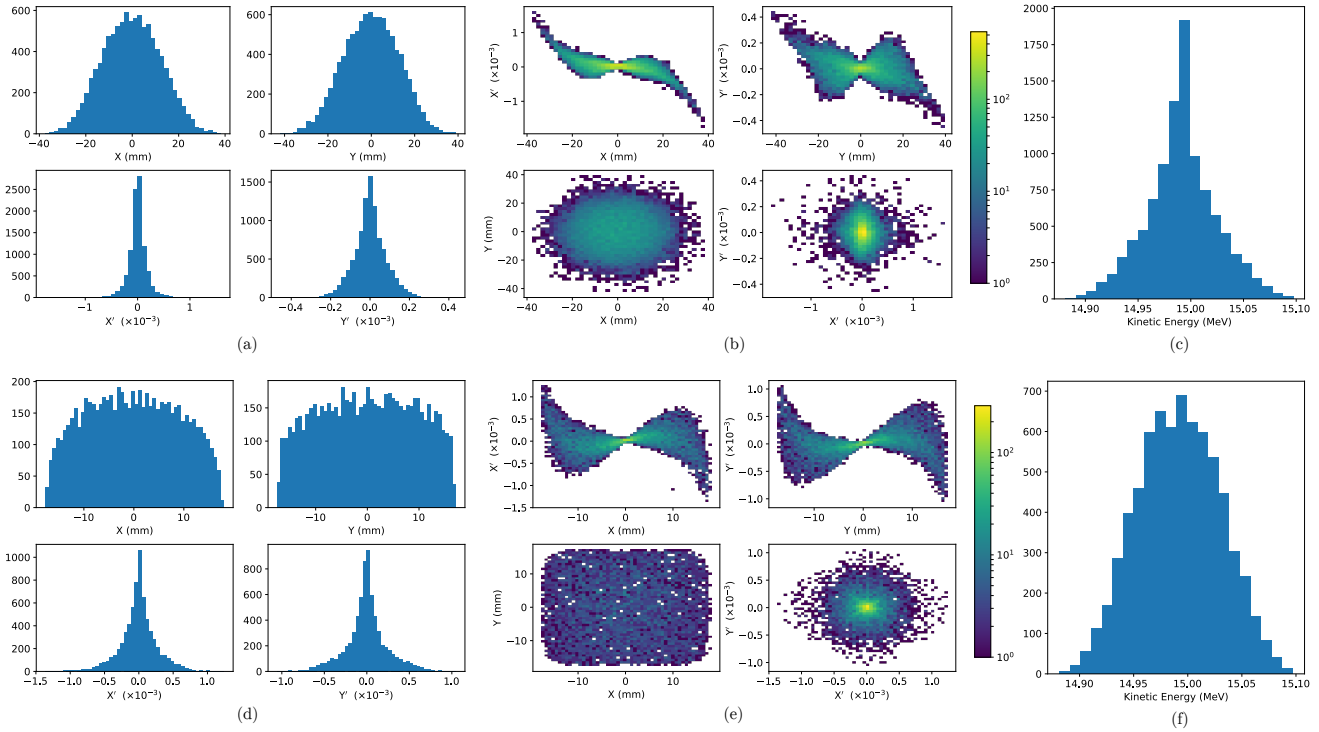


Figure 5. Beam phase space distributions at the end-station in the transverse plane, (X , Y); X' and Y' give the slope relative to the Z axis. The transverse phase space is shown in figures a and b for simulations without octupolar focusing and collimation, with the kinetic energy distribution shown in c. The same phase space distributions simulated with the effect of octupoles and collimation are in figures d, e, and f.

367 axes with and without beam shaping. Without octupoles, the spatial profile is Gaussian, as expected,
 368 however, beam uniformity is improved with octupoles and collimation. The total beam width is 3.58 cm
 369 horizontally and 3.46 cm vertically, which is sufficient to irradiate one well in a six-well cell-culture plate.
 370 Further optimisation is required to improve uniformity whilst optimising beam-line transmission, which is
 371 approximately 70% for the results presented in figure 5. An aberration can be seen in both transverse planes
 372 with and without beam shaping. This effect originates upstream of the octupoles in the solenoids, and
 373 persists through to the end station. These aberrations are a concern. Future simulation efforts will replace
 374 the solenoids with a full electromagnetic simulation of the Gabor lens. This change is likely to change the
 375 aberrations. The non-Gaussian energy distribution without beam shaping is a result of space-charge forces
 376 at the ion source; the distribution persists to the end station as no components which affect the longitudinal
 377 phase space were simulated. The Gaussian distribution seen with beam shaping is due to collimation.

378 The proposed design is capable of delivering beams of the desired size to the *in vitro* end station. Space-
 379 charge effects impact the beam-transport performance but it is believed that these can be mitigated with
 380 minor adjustments to the Gabor lenses in the capture section. Initial studies indicate that a uniform beam
 381 can be delivered with further optimisation of the octupoles and collimator.
 382

3.3.1 Alternative Design

384 To mitigate potential emittance growth from space-charge forces, an alternative beam line design was
 385 developed in which the final two Gabor lenses in the matching and energy selection section are replaced by
 386 four quadrupoles, limiting any bunch focusing to one plane at a time. The resulting machine is reduced

387 in length to 15.4 m. Without space-charge effects, a beam width of 2.5 mm at the end station can be
388 achieved. With space-charge, emittance growth prior to the first solenoid is once again observed leading
389 to an increased beam size at the entrance of the first quadrupole, resulting in a spatially asymmetric and
390 divergent beam at the end station. It is believed that the space-charge effects can be compensated by
391 applying the same Gabor-lens optimisation as in the baseline design and adjusting the quadrupole settings
392 to deliver beam parameters similar to those achieved in the absence of space charge. The alternative design
393 provides a solution that is more resilient to space-charge effects than the baseline, however, only the lower
394 bound on the desired beam size has been achieved so far. Further optimisation is required not only to
395 optimise optical performance but also to optimise octupole settings and to determine whether a beam with
396 the desired uniformity can be delivered to the end station.

397

398 3.4 Post-acceleration and beam delivery to the *in vitro* and *in vivo* end stations

399 A fixed-field alternating-gradient accelerator (FFA), based on the spiral scaling principle [Krest et al.
400 (1956); Symon et al. (1956); Fourrier et al. (2008); Tanigaki et al. (2006)], will be used to accelerate the
401 beam in LhARA Stage 2 to obtain energies greater than the 15 MeV protons and 4 MeV/u carbon (C^{6+})
402 ions delivered by the laser-driven source. FFAs have many advantages for both medical and radiobiological
403 applications such as: the capability to deliver high and variable dose; rapid cycling with repetition rates
404 ranging from 10 Hz to 100 Hz or beyond; and the ability to deliver various beam energies without the use
405 of energy degraders. An FFA is relatively compact due to the use of combined function magnets, which
406 lowers the overall cost compared to conventional accelerators capable of delivering beams at a variety of
407 energies such as synchrotrons. Extraction can be both simple and efficient and it is possible for multiple
408 extraction ports to be provided. Furthermore, FFAs can accelerate multiple ion species, which is very
409 important for radiobiological experiments and typically very difficult to achieve with cyclotrons.

410 A typical FFA is able to increase the beam momentum by a factor of three, though a greater factor may
411 be achieved. For LhARA, this translates to a maximum proton-beam energy of 127 MeV from an injected
412 beam of 15 MeV. For carbon ions (C^{6+}) with the same rigidity, a maximum energy of approximately
413 33.4 MeV/u can be produced.

414 The energy at injection into the FFA determines the beam energy at extraction. The injection energy will
415 be changed by varying the focusing strengths in the Stage 1 beam line from the capture section through to
416 the extraction line and the FFA ring. Appropriate adjustments to the frequency and phase of the RF in the
417 FFA ring will also be made. This will allow the appropriate energy slice from the broad energy spectrum
418 produced at the laser-driven source to be captured and transported to the FFA. The FFA will then accelerate
419 the beam, acting as a three-fold momentum multiplier. This scheme simplifies the injection and extraction
420 systems since their geometry and location can be kept constant.

421 A second, ‘high-energy’, *in vitro* end station will be served by proton beams with a kinetic energy in the
422 range 15–127 MeV and carbon-ion beams with energies up to 33.4 MeV/u. The extraction line from the
423 FFA leads to a 90° vertical arc to send the beam to the high-energy *in vitro* end station. If the first dipole of
424 the arc is not energised, the beam will be sent to the *in vivo* end station. The extraction line of the FFA
425 includes a switching dipole that will send the beam to the high-energy-beam dump if it is not energised.
426 The detailed design of the high-energy abort line, taking into account the requirement that stray radiation
427 does not enter the end stations, will be performed as part of the LhARA R&D programme.

428

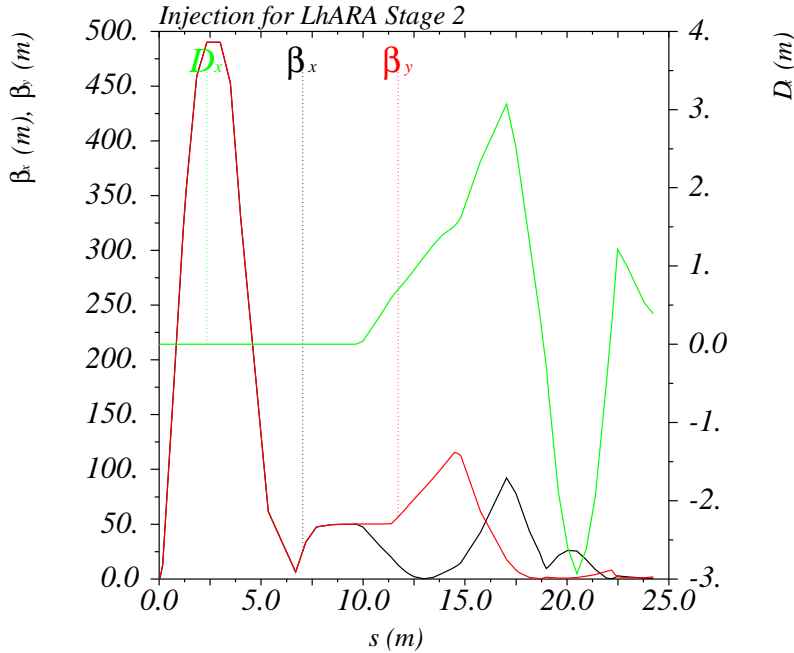


Figure 6. Twiss β_x and β_y functions and dispersion in the beam line consisting of the modified Stage 1 lattice and the transfer line allowing injection of the beam into the FFA ring. S goes from the laser target to the exit of the injection septum.

429 3.4.1 Injection line

430 The settings of the Stage 1 beam line need to be adjusted to reduce the Twiss β function propagating
 431 through the injection line to allow the beam to be injected into the FFA ring. The optical parameters in the
 432 Stage 1 beam line after adjustment are shown in figure 6. The beam is diverted by a switching dipole into
 433 the injection line which transports the beam to the injection septum magnet. The injection line matches
 434 the Twiss β functions in both transverse planes and the dispersion of the beam to the values dictated by
 435 the periodic conditions in the FFA cell (figure 6). The presence of dispersion in the injection line allows a
 436 collimator to be installed for momentum selection before injection. The beam is injected from the inside of
 437 the ring, which requires the injection line to cross one of the straight sections between the FFA magnets,
 438 see figure 7.

439

440 3.4.2 FFA ring

441 The magnetic field, B_y , in the median plane of a scaling spiral FFA is given by [Krest et al. (1956); Symon
 442 et al. (1956); Fourrier et al. (2008)]:

$$B_y = B_0 \left[\frac{R}{R_0} \right]^k F \left(\theta - \ln \left[\frac{R}{R_0} \right] \tan \zeta \right); \quad (3)$$

443 where B_0 is the magnetic field at radius R_0 , k is the field index, ζ corresponds to the spiral angle and F
 444 is the ‘flutter function’. This field law defines a zero-chromaticity condition, which means the working
 445 point of the machine is independent of energy up to field errors and alignment imperfections. This avoids
 446 crossing any resonances, which would reduce the beam quality and may lead to beam loss.

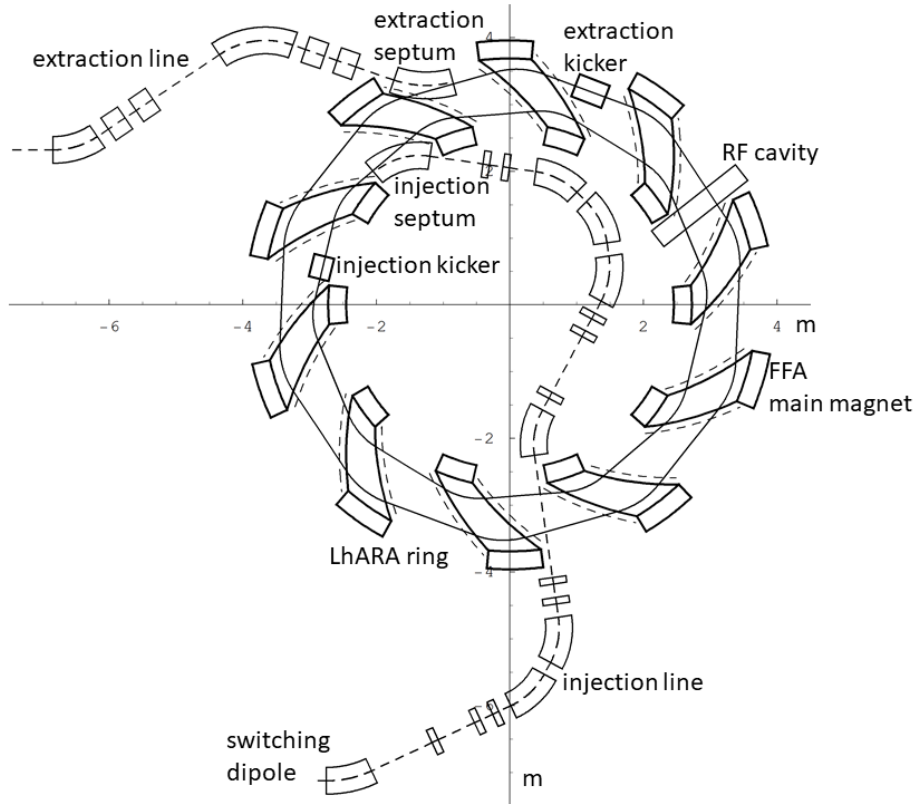


Figure 7. The layout of the injection line from the switching dipole to the injection septum together with the FFA ring, some of its subsystems and the first part of the extraction line.

447 Table 2 gives the main design parameters of the FFA ring. The ring consists of ten symmetric cells each
 448 containing a single combined-function spiral magnet. The choice of the number of cells is a compromise
 449 between the size of the orbit excursion, which dictates the radial extent of the magnet, and the length of the
 450 straight sections required to accommodate the injection and extraction systems.

451 The betatron functions and dispersion in one lattice cell at injection are shown in figure 8a. The tune
 452 diagram, showing the position of the working point of the machine in relation to the main resonance
 453 lines, is shown in figure 8b. Tracking studies were performed using a step-wise tracking code in which the
 454 magnetic field is integrated using a Runge-Kutta algorithm [Lagrange et al. (2018)]. The magnetic field in
 455 the median plane was obtained using the ideal scaling law (equation 3). Enge functions were used to give
 456 the fringe fields. The field out of the median plane was obtained using Maxwell's equations and a 6th-order
 457 Taylor expansion of the field. The dynamic acceptance for 100 turns, shown for the horizontal and vertical
 458 planes in figures 8c and 8d, respectively, are significantly larger than the beam emittance. This statement
 459 holds even if the most pessimistic scenario, in which the emittance is assumed to be ten times larger than
 460 nominal. These results confirm that a good machine working point has been chosen.

461 A full aperture, fast injection of the beam will be performed using a magnetic septum, installed on the
 462 inside of the ring, followed by a kicker magnet situated in a consecutive lattice cell, as shown in figure 7.
 463 The specifications of the injection system are dictated by the parameters of the beam at injection, which are
 464 summarised for the nominal proton beam in table 3. The beam at injection has a relatively small emittance
 465 and short bunch length, which limits the intensity accepted by the ring due to the space-charge effect. An
 466 intensity of approximately 10^9 protons will be accepted by the ring assuming the nominal beam parameters.

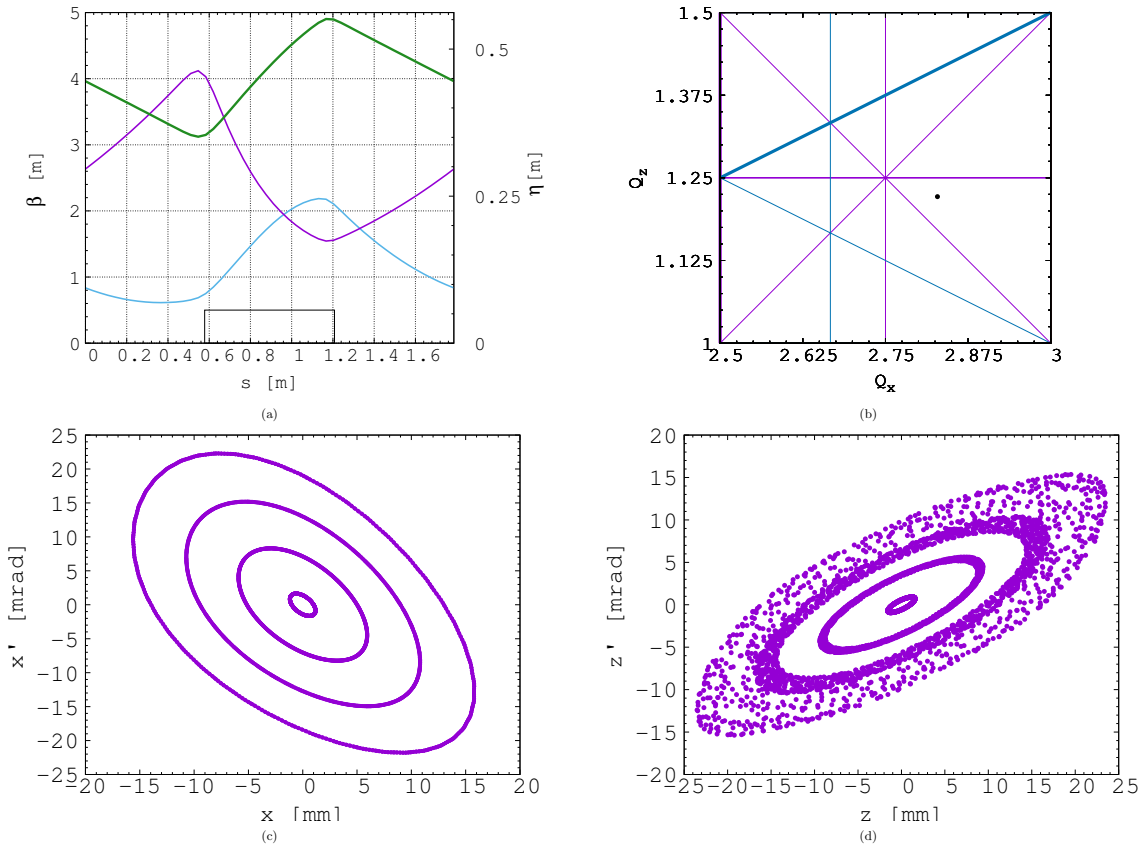


Figure 8. Beam optics and tracking in the FFA. Twiss β_h (blue), β_v (purple) functions and dispersion (green) in one lattice cell of the FFA ring (a). The working point of the FFA ring at (2.83, 1.22) on the tune diagram (b). The results of the horizontal (c) and vertical (d) dynamical acceptance study in the FFA ring, where a 1 mm offset is assumed in the vertical and horizontal planes respectively.

Table 3. Summary of the main parameters for the proton beam at the injection to the FFA ring. These parameters correspond to the nominal (maximum) acceleration mode of operation.

Parameter	Unit	Value
Beam energy	MeV	15
Total relative energy spread	%	± 2
Nominal physical RMS emittance (both planes)	$\pi \text{ m rad}$	4.1×10^{-7}
Incoherent space charge tune shift		-0.8
Bunching factor		0.023
Total bunch length	ns	8.1
Bunch intensity		10^9

467 Space-charge effects will be severe immediately after injection, but will quickly be reduced due to the
 468 debunching of the beam. Fast extraction of the beam over the full aperture will be performed using a kicker
 469 magnet followed by a magnetic septum installed in a consecutive lattice cell close to the extraction orbit.

470 Acceleration of the beam to 127 MeV will be done using an RF system operating at harmonic number
 471 $h = 1$ with an RF frequency range from 2.89 MHz to 6.48 MHz. The RF voltage required for 10 Hz
 472 operation is 0.5 kV. However, at such a low voltage the energy acceptance at injection will be limited to
 473 $\pm 0.7\%$ so a voltage of 4 kV is required to increase the energy acceptance to $\pm 2\%$. This voltage can be

Table 4. Beam emittance values and target β values for different beam sizes for 40 MeV and 127 MeV beams. The beam size is taken to be four times the sigma of the transverse beam distribution.

	40 MeV protons (Nominal)	127 MeV protons (Nominal)	127 MeV protons (Pessimistic)
RMS Emittance (ϵ_x, ϵ_y) [π mm mrad]	0.137	0.137	1.37
β [m] for a 1 mm spot size	0.46	0.46	0.039
β [m] for a 10 mm spot size	46	46	4.5
β [m] for a 30 mm spot size	410	410	40

474 achieved with one cavity [Yonemura et al. (2008)]. Here, two cavities are used to provide greater operational
 475 stability. Normal conducting spiral-scaling FFA magnets, similar to the ones needed for LhARA, have been
 476 constructed successfully [Tanigaki et al. (2006); Planche et al. (2009)] using either distributed, individually-
 477 powered coils on a flat pole piece or using a conventional gap-shaping technique. For the LhARA FFA, we
 478 propose a variation of the coil-dominated design recently proposed at the Rutherford Appleton Laboratory
 479 in R&D studies for the upgrade of the ISIS neutron and muon source. In this case, the nominal scaling field
 480 is achieved using a distribution of single-powered windings on a flat pole piece. The parameter k can then
 481 be tuned using up to three additional independently-powered windings. The extent of the fringe field across
 482 the radius of the magnet must be carefully controlled using a ‘field clamp’ to achieve zero-chromaticity.
 483 An active clamp, in which additional windings are placed around one end of the magnet, may be used to
 484 control the flutter function and thereby vary independently the vertical tune of the FFA ring. The FFA is
 485 required to deliver beams over a range of energy; each energy requiring a particular setting for the ring
 486 magnets. Therefore, a laminated magnet design may be required to reduce the time required to change the
 487 field. The magnet gap of 4.7 cm given in table 2 is estimated assuming a flat-pole design for the magnet.
 488

489 3.4.3 Extraction Line

490 Substantial margins in the beam parameters were assumed in the design of the extraction line from the
 491 FFA due to uncertainties in the beam distributions originating from: the Stage 1 beam transport; the
 492 FFA injection line; and potential distortions introduced by the presence of space-charge effects during
 493 acceleration in the ring. Therefore, the beam emittance was allowed, pessimistically, to be as large as a
 494 factor of ten greater than the nominal value, which was derived assuming that the normalised emittance
 495 is conserved from the source, through the Stage 1 beam line, and in the FFA ring. In the nominal case,
 496 the physical emittance of the beam is affected by adiabatic damping only. Substantial flexibility in the
 497 optics of the extraction line is required, as the extraction line must accommodate a wide spectrum of beam
 498 conditions to serve the *in vitro* and *in vivo* end-stations.

499 Detailed studies were carried out for proton beams with kinetic energies of 40 MeV and 127 MeV. Table
 500 4 gives the Twiss β values for different beam sizes for the 40 MeV and 127 MeV proton-beam scenarios
 501 assuming a Gaussian beam distribution. The optics and geometric acceptance of the system is approximately
 502 the same for the 40 MeV and 127 MeV beams. This justified the working hypothesis that beam emittance is
 503 approximately the same for both beam energies. This assumption will be revised as soon as space-charge
 504 simulations for the entire system are available.

505 The first two dipoles and four quadrupoles of the extraction line bend the beam coming from the extraction
 506 septum of the FFA such that it is parallel to the low-energy beam line while ensuring that dispersion is
 507 closed. Closing the dispersion is critical as off-momentum particles will follow trajectories different to
 508 those followed by particles with the design momentum and therefore impact the size and shape of the beam

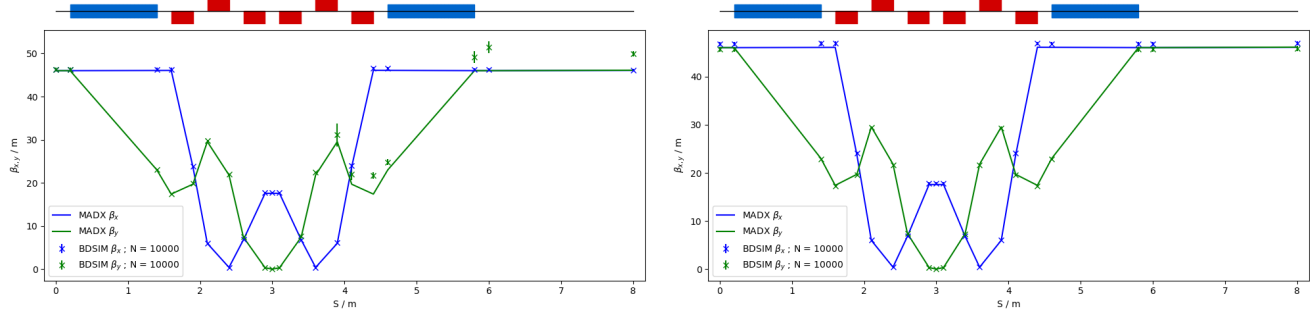


Figure 9. Comparison of MAD-X and BDSIM simulation of 40 MeV (left) and nominal 127 MeV (right) proton beam passing through the high energy *in vitro* arc simulated with 10^4 particles (in BDSIM).

509 downstream. The second part of the extraction line consists of four quadrupoles which transport the beam
 510 either to the first dipole of the vertical arc that serves the high-energy *in vitro* end station or to the *in vivo*
 511 end-station if this dipole is not energised. These quadrupoles provide the flexibility required to produce the
 512 different beam sizes for the *in vitro* end station as specified in table 4.

513

514 3.4.4 High-energy *in vitro* beam line

515 The high-energy *in vitro* beam line transports the beam from the exit of the extraction line and delivers it to
 516 the high-energy *in vitro* end station. The 90° vertical bend is a scaled version of the low-energy vertical arc,
 517 following the same design principles, and also consists of two bending dipole magnets and six quadrupole
 518 magnets. To accommodate the higher beam energies, the lengths of the magnets were scaled in order to
 519 ensure that peak magnetic fields were below the saturation limits of normal conducting magnets. The
 520 bending dipole magnet lengths were increased to 1.2 m each and the quadrupole lengths were tripled to
 521 0.3 m each. The overall length of the arc then becomes 6 m, compared to 4.6 m for the low energy *in vitro*
 522 arc. This difference in arc length means the high-energy *in vitro* arc finishes about 0.9 m higher than the
 523 low-energy one. This difference can easily be accommodated by adjusting the final drift lengths.

524 The quadrupole strengths for the scaled high-energy *in vitro* arc were obtained using MADX and tracking
 525 simulations using BDSIM show good agreement, see figure 9. The input beam distribution used in BDSIM
 526 was assumed to be Gaussian with Twiss $\beta = 46$, which gives a beam size of about 10 mm. Small deviations
 527 from the BDSIM results were observed in GPT simulations due to space-charge effects.

528

529 3.4.5 *In vivo* beam line

530 To facilitate efficient small-animal handling, an end station dedicated to *in vivo* experiments has been
 531 positioned adjacent to the principle road access to the facility. If the first dipole of the high-energy *in vitro*
 532 arc is not energised, the beam is sent to the *in vivo* end station. From the end of the extraction line, 7.7 m of
 533 drift is necessary to clear the first bending dipole of the *in vitro* arc, to provide space for the five RF cavities
 534 needed for longitudinal phase-space manipulation and to allow space for diagnostic devices. Following this
 535 drift is a further 6.6 m of beam line that includes four quadrupoles, each of length 0.4 m, which are used to
 536 perform the final focusing adjustments of the beam delivered to the *in vivo* end station. A final 1.5 m drift
 537 length at the end is reserved for scanning magnets to be installed to perform spot scanning and to penetrate
 538 the shielding of the *in vivo* end station. In total the *in vivo* beam line is 15.6 m in length.

539 The design is flexible in matching the various $\beta_{x,y}$ values given in table 4, but is not able to match the
 540 smallest target value of $\beta_{x,y} = 0.039$ m for the pessimistic scenario, which is very challenging. To verify

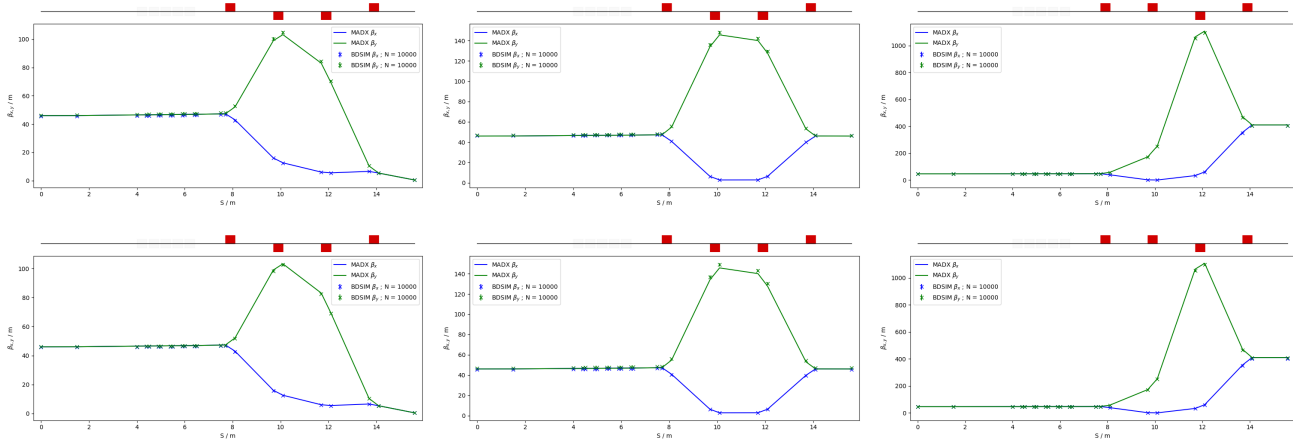


Figure 10. MAD-X and BDSIM simulations of the *in vivo* beam line for a 40 MeV proton beam (top row) and a nominal 127 MeV proton beam (bottom row) with quadrupoles matched to $\beta_{x,y} = 0.46$ m (left), $\beta_{x,y} = 46$ m (middle) and $\beta_{x,y} = 410$ m (right) for 10^4 particles.

541 that the optics design could provide the required beam sizes, simulations were performed with BDSIM
 542 using an input Gaussian beam generated with the Twiss β values given in tables 4. Figure 10 shows the
 543 results of simulations for a 40 MeV proton beam and a nominal emittance 127 MeV proton beam matched
 544 in order to obtain beam sizes of 1 mm, 10 mm and 30 mm.
 545

546 3.5 Instrumentation

547 Commercial off-the-shelf (COTS) instrumentation will be used for Stages 1 and 2 of LhARA wherever
 548 possible. However, the characteristics of the beam (e.g. very high charge-per-bunch, low-to-moderate
 549 energy) will require some custom solutions to be developed. The authors are developing two concepts,
 550 termed SciWire and SmartPhantom, for the low- and high-energy *in vitro* end stations respectively. These
 551 detectors can also be used for beam diagnostics. This new instrumentation may find application at other
 552 facilities. Instrumentation for the detection of secondary particles arising from the interaction of the beam
 553 with tissue is not discussed here but is an important area that will be studied in the future.
 554

555 3.5.1 SciWire

556 For the Stage 1 beam, the maximum proton energy is 15 MeV. Shot-to-shot characterisation of the beam is
 557 essential and requires the use of a very thin detector with a fast response. The SciWire [Kurup (2019)] is
 558 being developed to provide energy and intensity profile measurements for low-energy ion beams. A single
 559 SciWire plane consists of two layers of 250 μm square-section scintillating fibres, with the fibre directions
 560 in the two layers orthogonal to each other. A series of back-to-back planes provides a homogeneous volume
 561 of scintillator. If there are enough planes to stop the beam, the depth of penetration will allow the beam
 562 energy to be inferred. This is obviously a destructive measurement so would only be performed when
 563 experiments are not running. A single plane, however, can be used for 2D beam-profile measurements at
 564 the same time that beam is delivered for experiments. Detection of the light from SciWire fibres may be by
 565 CMOS camera, or using photodiodes. If the instrumentation is sufficiently fast, the SciWire can be used to
 566 derive feedback signals for beam tuning.

567

568 3.5.2 SmartPhantom

569 To study in real time the dose profile of Stage 2 beams, the SmartPhantom [Barber (2018)] is being
570 developed. This is a water-filled phantom, instrumented with planes of scintillating fibres, used to infer
571 the dose distribution with distance. The detection elements of the SmartPhantom are 250 µm diameter,
572 round, scintillating fibres. Each fibre station consists of two planes of fibres, in which the fibre directions
573 are orthogonal. Five fibre stations are arranged in the phantom in front of the cell-culture flask. The fibres
574 may be coupled to photodiodes, or a CMOS camera. Simulations in GEANT4 are being used to develop
575 analysis techniques to determine the position of the Bragg peak shot-by-shot. The beam profile and dose
576 delivered can then be calculated in real time.

577 3.5.3 Beam line Instrumentation

578 The instrumentation requirement begins with the Ti:Sapphire laser. The laser focal spot will be characterised
579 using a camera-based system and high-speed wavefront measurements [Wang (2014)] from COTS vendors.

581 For the Stage 1 beam line, beam position monitors (BPMs) will be needed for beam steering. Because
582 of the low beam energy, non-intercepting BPMs using capacitive pickup buttons will be used. Custom
583 pickups will be needed to match the beam pipe geometry but COTS electronics are available. The beam
584 current will be monitored near the end of each beam line, using integrating current toroids (ICT), backed
585 up with the option of insertable multi-layer Faraday cups (MLFC) to give absolute beam current and energy
586 measurements. Beam profiles could be measured by SEM grids on both Stage 1 and Stage 2 beam lines.
587 For Stage 1, these monitors will be mounted on pneumatic actuators to avoid scattering. Each end station
588 could be equipped with insertable “pepper-pot” emittance monitors and a transverse deflection cavity with
589 fluorescent screen could be provided for bunch shape measurements.

590 The BPMs on the FFA will require pickup designs suitable for the unusual, wide and shallow vacuum
591 vessel. The FFA at the KURNS facility in Kyoto is of a similar layout [Uesugi (2018)] and uses a kicker
592 and capacitive pickup to perform tune measurements in each transverse direction. A minimum of one BPM
593 every second cell will be used in the FFA so that the beam orbit can be measured. BPMs will also be
594 required close to the injection and extraction septa. The BPM system may be able to use COTS electronics,
595 but the pickups will be based on the KURNS design of multiple electrodes arranged across the vacuum
596 vessel width.

597 The data acquisition system needs to be able to store calibration data and apply corrections in real time. It
598 is necessary to be able to find the beam centre from a profile, even when the profile may be non-Gaussian
599 and possibly asymmetric. Field programmable gate arrays (FPGAs) can be used to perform fast fitting and
600 pattern recognition of beam profiles. The instrumentation will be integrated with the accelerator control
601 system to be able to provide fast feedback and adjustment of the beam parameters in real time.

602 603 3.6 Biological end stations

604 In order to deliver a successful radiobiological research programme, high-end and fully equipped *in vitro*
605 and *in vivo* end-stations will be housed within the LhARA facility. The two *in vitro* end-stations (high
606 and low energy) will contain vertically-delivered beam lines which will be used for the irradiation of 2D
607 monolayer and 3D-cell systems (spheroids and patient-derived organoids) in culture. The beam line within
608 the end-stations will be housed in sealed units that will be directly sourced with appropriate gases (carbon
609 dioxide and nitrogen), allowing for the cells within culture plates to be incubated for a short time in stable
610 conditions prior to and during irradiation. This will also enable the chamber to act, where necessary, as a

611 hypoxia unit (0.1%–5% oxygen concentration). Furthermore, these sealed units will contain robotics to
612 enable the numerous cell culture plates housed within to be placed into and taken out of the beam.

613 The *in vitro* end-stations will be located within a research laboratory equipped with up-to-date and
614 state-of-the-art facilities. The laboratory will include all the vital equipment for bench-top science, sample
615 processing and analysis (e.g. refrigerated centrifuges and light/fluorescent microscopes), along with the
616 equipment required for contaminant-free cell culture (e.g. humidified CO₂ cell culture incubators, Class II
617 biological safety cabinets), and for the storage of biological samples and specimens (e.g. –20°C and –80°C
618 freezers and fridges). The laboratory will also house an X-ray irradiator (allowing direct RBE comparisons
619 between conventional photon irradiation, and the proton and carbon ions delivered by the accelerator),
620 hypoxia chamber (for long-term hypoxia studies), a robotic workstation (handling and processing of large
621 sample numbers, assisting in high-throughput screening experiments), and an ultra-pure-water delivery
622 system. These facilities will enable a myriad of biological end-points to be investigated in both normal- and
623 tumour-cell models not only from routine clonogenic survival and growth assays, but also from significantly
624 more complex end-points (e.g. inflammation, angiogenesis, senescence and autophagy).

625 The *in vivo* end-station will be served with high-energy proton and carbon ions capable of penetrating
626 deeper into tissues allowing the irradiation of whole animals. The ability to perform *in vivo* pre-clinical
627 studies is vital for the future effective translation of the research into human cancer patients where optimum
628 treatment strategies and the reduction of side-effects are crucial. The *in vivo* end-station will allow the
629 irradiation of a number of small-animal models (e.g. xenograft mouse and rat models) which can further
630 promote an examination of particular ions on the appropriate biological end-points (e.g. tumour growth
631 and normal tissue responses). The end-station will contain a small-animal handling area which will allow
632 for the anaesthetisation of animals prior to irradiation. To enable the irradiation of small target volumes
633 with a high level of precision and accuracy, an image guidance system (e.g. computed tomography) will be
634 available. The animals will subsequently be placed in temperature-controlled holder tubes enabling the
635 correct positioning of the relevant irradiation area in front of the beam line. The beam size is sufficient to
636 give flexibility in the different irradiation conditions, in particular through passive scattering, pencil-beam
637 scanning, and micro-beam irradiation, to be investigated at both conventional and FLASH dose rates. It is
638 envisaged that the animals will be taken off-site post-irradiation to a nearby animal-holding facility for a
639 follow-up period where biological measurements will be conducted.
640

641 **3.7 Infrastructure and integration**

642 The LhARA facility will encompass two floors of roughly 42 m in length and 18 m wide. The ground floor
643 will contain the laser, accelerator, and *in vivo* end station while the first floor will house the laboratory area
644 and the two *in vitro* end stations. The entire facility will require radiation protection in the form of concrete
645 shielding. There will be three principal areas: a radiation controlled-access area, a laser controlled-access
646 area, and a laboratory limited-access area.

647 For a facility such as LhARA, laser, radiation and biological safety are primary concerns. It is envisaged
648 that LhARA will be built at a national Laboratory or equivalent research institute which has an established
649 safety-management system and culture in place.

650 The infrastructure and integration of the LhARA facility will require R&D in four key areas: risk analysis
651 (project risks), risk assessments (safety risks), radiation simulations, and controls development. The risk
652 analysis will cover all aspects of the facility, such as funding and resource availability, not just technical
653 risks. A safety-risk assessment will be performed to describe and control all potential safety risks in the

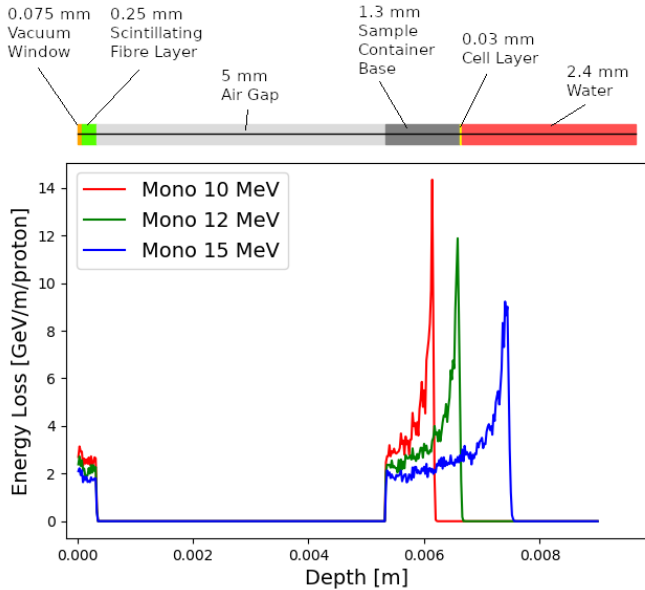


Figure 11. Energy loss as a function of depth in the low-energy *in vitro* end station for three mono-energetic proton energies: 10 MeV; 12 MeV; and 15 MeV. Each beam was simulated using 10^4 particles at the start of the simulated end station. The material through which the beam passes is indicated above the figure. The entrance window is plotted at a Depth value of 0 m. The beam deposits energy in the beam window and the layer of scintillating fibre before passing through the air and entering the sample container.

654 facility. The safety-risk assessment will, to a reasonable degree, identify all pieces of equipment that
 655 require safety mitigations and identify control measures that must be put in place. Coupled closely with the
 656 safety-risk assessment, radiation simulations will be developed to characterise the radiation hazards in and
 657 around the LhARA facility. The last area to require R&D will be the control systems. It is expected that the
 658 facility will use the Experimental Physics and Industrial Control System, which can be further developed
 659 at this stage.
 660

4 PERFORMANCE

661 The dose distributions delivered to the end stations were evaluated using BDSIM. Figure 11 shows the
 662 energy lost by the beam as it enters the low-energy *in vitro* end station. The beam passes through the
 663 vacuum window, a layer of scintillating fibre, and a 5 mm air gap. The beam then enters the cell-sample
 664 container, assumed to be polystyrene, which supports a $30\ \mu\text{m}$ thick layer of cells, modelled using the
 665 Geant4 material "G4_SKIN_ICRP" [NIST (2017)]. The transverse momentum of protons in the beam was
 666 assumed to be Gaussian distributed, with a lateral spread small enough for the beam to be fully contained
 667 within the required spot size of 3 cm. Figure 11 shows that a proton beam with 10 MeV kinetic energy
 668 does not reach the cell. The Bragg peak of a 12 MeV proton beam is located close to the cell layer, while
 669 a 15 MeV beam, the maximum energy specified for delivery to the low-energy *in vitro* end station, has
 670 a Bragg peak located beyond the cell layer. LhARA's ability to deliver various energies will allow the
 671 investigation of radiobiological effects for irradiations using different parts of the Bragg peak, effectively
 672 varying the LET across the sample. RF cavities are placed in both the stage 1 and the stage 2 beam lines to
 673 allow the manipulation of the energy of the bunch as a function of time. This facility will allow the study
 674 of the impact of a "spread-out Bragg peak" (SOBP).

675 The maximum dose that can be delivered was evaluated for a variety of beam energies. In order for
676 the dose to be reported in units of Gray it is necessary to define the volume within which the energy
677 deposition is to be integrated. Therefore, the dose was estimated from simulations by calculating the energy
678 deposited in a volume of water corresponding in size to the sensitive volume of a PTW 23343 Markus ion
679 chamber [PTW (2019/2020)] placed at the position of the Bragg peak in each case. This choice allows the
680 doses and dose-rates reported below to be compared to other facilities which are in operation, since the
681 PTW 23343 Markus ion chamber is widely used at existing facilities. The cylindrical sensitive volume of
682 the ion chamber has a radius of 2.65 mm and a depth of 2 mm, giving a volume of about $4.4 \times 10^{-8} \text{ m}^3$.
683 The total energy deposited within the chamber was recorded and converted into dose in units of Gray.

684 For the low-energy *in vitro* end station, the minimum spot size is specified to have a diameter of 10 mm,
685 which is larger than the area of the chamber. A single shot of 10^9 protons at 12 MeV with the minimum
686 design spot size deposits $3.1 \times 10^{-4} \text{ J}$ in the chamber volume, corresponding to a dose of 7.1 Gy. For this
687 simulation, the thickness of the sample container was reduced so that the Bragg peak could be positioned
688 within the chamber volume. For the bunch length of 7.0 ns, the maximum instantaneous dose rate is
689 $1.0 \times 10^9 \text{ Gy/s}$ and the average dose rate is 71 Gy/s, assuming a repetition rate of 10 Hz. A single shot of
690 10^9 protons at 15 MeV deposits $5.6 \times 10^{-4} \text{ J}$ in the chamber volume, corresponding to a dose of 12.8 Gy.
691 This gives an instantaneous dose rate of $1.8 \times 10^9 \text{ Gy/s}$ and an average dose rate of 128 Gy/s assuming the
692 same bunch length and repetition rate as for the 12 MeV case.

693 For the high-energy *in vitro* end station, a different setup was used for high energy proton beams. A
694 similar design to the low-energy end station was used but with the air gap increased from 5 mm to 5 cm and
695 a water phantom was placed at the end of the air gap instead of a cell culture plate. The water phantom
696 used in the simulation was based upon the PTC T41023 water phantom [PTW (2009)]. In addition, the
697 smaller minimum design beam size of 1 mm was used. A single shot of 10^9 protons at 127 MeV deposits
698 $6.9 \times 10^{-4} \text{ J}$ in the chamber at the pristine Bragg peak depth corresponding to a dose of 15.6 Gy, an
699 instantaneous dose rate of $3.8 \times 10^8 \text{ Gy/s}$ and an average dose rate of 156 Gy/s. The end-station design
700 assumed for a 33.4 MeV/u carbon beam was the same as that used for the low-energy *in vitro* end station
701 due to the limited range in water of the carbon beam. The intensity of the beam is a factor of 12 less than
702 for protons in order to preserve the same strength of the space-charge effect at injection into the FFA with
703 the same beam parameters, as the incoherent space charge tune shift is proportional to q^2/A and inversely
704 proportional to $\beta^2\gamma^3$, where q corresponds to the particle charge, A its mass number, and β and γ its
705 relativistic parameters. A single pulse of 8.3×10^7 ions deposits $3.2 \times 10^{-3} \text{ J}$ at the depth of the pristine
706 Bragg peak, leading to an instantaneous dose rate of $9.7 \times 10^8 \text{ Gy/s}$ and a maximum average dose rate of
707 730 Gy/s.

708 The expected maximum dose rates are summarised in table 5. The instantaneous dose rates depend on the
709 bunch length which differs depending on the energies. For the low-energy *in vitro* line, a 7 ns bunch length
710 is assumed for all energies. For the higher energies, a 127 MeV proton beam is delivered with a bunch
711 length of 41.5 ns, and a bunch length of 75.2 ns for a 33.4 MeV/u carbon beam. The same repetition rate of
712 10 Hz was used for all energies. The minimum beam size at the start of the end station for the 12 MeV and
713 15 MeV proton-beam simulations was 1 cm. A 1 mm beam size was used for the 127 MeV proton beam and
714 33.4 MeV/u carbon-ion beam simulations.

715

Table 5. Summary of expected maximum dose per pulse and dose rates that LhARA can deliver for minimum beam sizes. These estimates are based on Monte Carlo simulations using a bunch length of 7 ns for 12 MeV and 15 MeV proton beams, 41.5 ns for the 127 MeV proton beam and 75.2 ns for the 33.4 MeV/u carbon beam. The average dose rate is based on the 10 Hz repetition rate of the laser source.

	12 MeV Protons	15 MeV Protons	127 MeV Protons	33.4 MeV/u Carbon
Dose per pulse	7.1 Gy	12.8 Gy	15.6 Gy	73.0 Gy
Instantaneous dose rate	1.0×10^9 Gy/s	1.8×10^9 Gy/s	3.8×10^8 Gy/s	9.7×10^8 Gy/s
Average dose rate	71 Gy/s	128 Gy/s	156 Gy/s	730 Gy/s

5 CONCLUSIONS

The initial conceptual design of LhARA, the Laser-hybrid Accelerator for Radiobiological Applications, has been described and its performance evaluated in simulations that take into account the key features of the facility. LhARA combines a laser-driven source to create a large flux of protons or light ions which are captured and formed into a beam by strong-focusing plasma lenses thus evading the current space-charge limit on the instantaneous dose rate that can be delivered. Acceleration, performed using a fixed-field alternating-gradient accelerator, preserves the unique flexibility in the time, spectral, and spatial structure of the beam afforded by the laser-driven source. The ability to trigger the laser pulse that initiates the production of protons or ions at LhARA will allow the time structure of the beam to be varied to interrupt the chemical and biological pathways that determine the biological response to ionising radiation. In addition, the almost parallel beam that LhARA will deliver can be varied to illuminate a circular area with a maximum diameter of between 1 cm and 3 cm with an almost uniform dose or focused to a spot with diameter of ~ 1 mm. These features make LhARA the an extremely flexible tool for the systematic study of the radiobiology of proton and ion beams.

The laser-hybrid approach, therefore, will allow radiobiological studies and eventually radiotherapy to be carried out in completely new regimes, delivering a variety of ion species in a broad range of time structures and spatial configurations at instantaneous dose rates up to and potentially significantly beyond the current ultra-high dose-rate “FLASH” regime. By demonstrating a triggerable system that incorporates dose-deposition imaging in the fast feedback-and-control system. In the long term, LhARA has the potential to remove the requirement for a large gantry and so lay the foundations for “best in class” treatments to be made available to the many by reducing the footprint of future particle-beam therapy systems.

LhARA has the potential to drive a change in clinical practice in the medium term by increasing the wealth of radiobiological knowledge. This enhanced understanding in turn may be used to devise new approaches to decrease radio-toxicity on normal tissue while maintaining, or even enhancing, the tumour control probability. The radiobiology programme in combination with the demonstration in operation of the laser-hybrid technique means that the execution of the LhARA programme has the potential to drive a step-change in the clinical practice of proton- and ion-beam therapy.

ACKNOWLEDGEMENTS

The work described here was made possible by a grant from the Science and Technology Facilities Council (ST/T002638/1, ST/P002021/1). Additional support was provided by the STFC Rutherford Appleton and Daresbury Laboratories and members of the LhARA consortium. We gratefully acknowledge all sources of support. A pre-publication review of the pre-CDR for LhARA was carried out by P. Bolton (LMU,

747 Munich), M. Lamont (CERN), Y. Prezado (Institut Curie), and F. Romano (INFN-LNS and the National
748 Physical Laboratory). We are grateful to the review panel for their support and detailed feedback on the
749 draft pre-CDR.
750

REFERENCES

- 751 (2009). *User Manual Water Phantom T41023*. PTW-Freiburg Physikalisch-Technische Werkstatten Dr.
752 Pychlau GmbH, d738.131.00/02 en edn.
753 (2019/2020). *Ionizing Radiation Detectors*. PTW-Freiburg Physikalisch-Technische Werkstatten Dr.
754 Pychlau GmbH
755 [Dataset] (2020). Vsim for plasma. <https://www.txcorp.com/vsim>
756 [Dataset] A-SAIL Project (2020). A-sail project. <https://www.qub.ac.uk/research-centres/A-SAILProject/>
757
758 Amin, T., Barlow, R., Ghithan, S., Royb, G., and Schuhb, S. (2018). Formation of a uniform ion beam
759 using octupole magnets for biolir facility at cern. *JINST* 13, P04016
760 Atun, R., Jaffray, D. A., Barton, M. B., Bray, F., Baumann, M., Vikram, B., et al. (2015). Expanding
761 global access to radiotherapy. *The Lancet Oncology* 16, 1153 – 1186. doi:[https://doi.org/10.1016/S1470-2045\(15\)00222-3](https://doi.org/10.1016/S1470-2045(15)00222-3)
762
763 Autin, B., Carli, C., D'Amico, T., Gröbner, O., Martini, M., and Wildner, E. (1998). *BeamOptics: A program for analytical beam optics*. Tech. Rep. CERN-98-06, European Organization for
764 Nuclear Research (CERN). http://inis.iaea.org/search/search.aspx?orig_q=RN:30052986
765
766 Barber, G. (2018). Outline design and cost estimate for the SmartPhantom. *Unpublished note*
767 Berry, R. J. (1973). EFFECTS OF RADIATION DOSE-RATE: From Protracted, Continuous Irradiation
768 to Ultra-High Dose-Rates from Pulsed Accelerators. *British Medical Bulletin* 29, 44–47. doi:[10.1093/oxfordjournals.bmb.a070955](https://doi.org/10.1093/oxfordjournals.bmb.a070955)
769
770 Bin, J., Allinger, K., Assmann, W., Dollinger, G., Drexler, G. A., Friedl, A. A., et al. (2012). A laser-
771 driven nanosecond proton source for radiobiological studies. *Applied Physics Letters* 101, 243701.
772 doi:[10.1063/1.4769372](https://doi.org/10.1063/1.4769372)
773
774 Bin, J., Ma, W., Wang, H., Streeter, M., Kreuzer, C., Kiefer, D., et al. (2015). Ion Acceleration Using
775 Relativistic Pulse Shaping in Near-Critical-Density Plasmas. *Physical Review Letters* 115, 064801.
776 doi:[10.1103/PhysRevLett.115.064801](https://doi.org/10.1103/PhysRevLett.115.064801)
777 Bourhis, J., WJ, S., PG, J., O, G., C, B., F, D., et al. (2019). Treatment of a first patient with FLASH-
778 radiotherapy. *Radiotherapy and oncology : journal of the European Society for Therapeutic Radiology
779 and Oncology* 139. doi:[10.1016/J.RADONC.2019.06.019](https://doi.org/10.1016/J.RADONC.2019.06.019)
780 Bray, F., Ferlay, J., Soerjomataram, I., Siegel, R. L., Torre, L. A., and Jemal, A. (2018). Global cancer
781 statistics 2018: GLOBOCAN estimates of incidence and mortality worldwide for 36 cancers in 185
782 countries. *CA: A Cancer Journal for Clinicians* 68, 394–424. doi:[10.3322/caac.21492](https://doi.org/10.3322/caac.21492)
783 Bulanov, S., Esirkepov, T., Khoroshkov, V., Kuznetsov, A., and Pegoraro, F. (2002). Oncological
784 hadrontherapy with laser ion accelerators. *Physics Letters A* 299, 240–247. doi:[https://doi.org/10.1016/S0375-9601\(02\)00521-2](https://doi.org/10.1016/S0375-9601(02)00521-2)
785
786 Carter, R. J., Nickson, C. M., Thompson, J. M., Kacperek, A., Hill, M. A., and Parsons, J. L. (2018). Complex dna damage induced by high linear energy transfer alpha-particles and protons triggers a
787 specific cellular dna damage response. *International Journal of Radiation Oncology*Biology*Physics*
788 100, 776 – 784. doi:<https://doi.org/10.1016/j.ijrobp.2017.11.012>
789

- 790 Chaudhary, P., Gwynne, D., Doria, D., Romagnani, L., Maiorino, C., Padda, H., et al. (2017). Effectiveness
791 of laser accelerated ultra high dose rate protons in DNA DSB damage induction under hypoxic conditions.
792 In *44th EPS Conference on Plasma Physics, EPS 2017* (European Physical Society (EPS)), vol. 44F.
793 P1.217
- 794 Chaudhary, P., Marshall, T. I., Perozziello, F. M., Manti, L., Currell, F. J., Hanton, F., et al. (2014). Relative
795 Biological Effectiveness Variation Along Monoenergetic and Modulated Bragg Peaks of a 62-MeV
796 Therapeutic Proton Beam: A Preclinical Assessment. *International Journal of Radiation Oncology •*
797 *Biology • Physics* 90, 27–35. doi:10.1016/j.ijrobp.2014.05.010
- 798 Chen, S. N., Vranic, M., Gangolf, T., Boella, E., Antici, P., Bailly-Grandvaux, M., et al. (2017). Collimated
799 protons accelerated from an overdense gas jet irradiated by a $1\text{ }\mu\text{m}$ wavelength high-intensity short-pulse
800 laser. *Scientific Reports* 7, 13505. doi:10.1038/s41598-017-12910-6
- 801 Cirrone, G., Catalano, R., Cuttone, G., Margarone, D., Schillaci, F., and Petringa, G. (2020). Generation
802 control and application of flash radiation beam from laser-matter interaction: The ELIMAIA-ELIMED
803 beamline. *Nuovo Cim. C* 43, 15. doi:10.1393/ncc/i2020-20015-6
- 804 Cirrone, G. et al. (2016). Status, Plans and Potential Applications of the ELIMED Beam Line at
805 ELI-Beamlines. In *7th International Particle Accelerator Conference*. WEXB01. doi:10.18429/
806 JACoW-IPAC2016-WEXB01
- 807 Cirrone, G. A. P., Margarone, D., Maggiore, M., Anzalone, A., Borghesi, M., Jia, S. B., et al. (2013).
808 ELIMED: a new hadron therapy concept based on laser driven ion beams. In *Laser Acceleration of*
809 *Electrons, Protons, and Ions II; and Medical Applications of Laser-Generated Beams of Particles II;*
810 *and Harnessing Relativistic Plasma Waves III*, eds. E. Esarey, C. B. Schroeder, W. P. Leemans, K. W. D.
811 Ledingham, and D. A. Jaroszynski. International Society for Optics and Photonics (SPIE), vol. 8779,
812 216 – 225. doi:10.1117/12.2026530
- 813 Clark, E. L., Krushelnick, K., Davies, J. R., Zepf, M., Tatarakis, M., Beg, F. N., et al. (2000a). Measurements of energetic proton transport through magnetized plasma from intense laser interactions
814 with solids. *Phys. Rev. Lett.* 84, 670–673. doi:10.1103/PhysRevLett.84.670
- 815 Clark, E. L., Krushelnick, K., Zepf, M., Beg, F. N., Tatarakis, M., Machacek, A., et al. (2000b). Energetic
816 heavy-ion and proton generation from ultraintense laser-plasma interactions with solids. *Phys. Rev. Lett.*
817 85, 1654–1657. doi:10.1103/PhysRevLett.85.1654
- 818 Daido, H., Nishiuchi, M., and Pirozhkov, A. S. (2012). Review of laser-driven ion sources and their
819 applications. *Reports on Progress in Physics* 75, 56401. doi:10.1088/0034-4885/75/5/056401
- 820 Datta, N. R., Rogers, S., and Bodis, S. (2019). Challenges and Opportunities to Realize “The 2030 Agenda
821 for Sustainable Development” by the United Nations: Implications for Radiation Therapy Infrastructure
822 in Low- and Middle-Income Countries. *International Journal of Radiation Oncology*Biology*Physics*
823 105, 918–933. doi:<https://doi.org/10.1016/j.ijrobp.2019.04.033>
- 824 De Loos, M. J. and Van der Geer, S. B. (1996). General Particle Tracer: A New 3D Code for Accelerator
825 and Beamline Design
- 826 deGrassie, J. S. and Malmberg, J. H. (1980). Waves and transport in the pure electron plasma. *The Physics*
827 *of Fluids* 23, 63–81. doi:10.1063/1.862864
- 828 Doria, D., Kakolee, K. F., Kar, S., Litt, S. K., Fiorini, F., Ahmed, H., et al. (2012). Biological effectiveness
829 on live cells of laser driven protons at dose rates exceeding 10^9 Gy/s . *AIP Advances* 2, 011209.
830 doi:10.1063/1.3699063
- 831 Dover, N., Nishiuchi, M., Sakaki, H., Kondo, K., Lowe, H., Alkhimova, M., et al. (2020). Demonstration
832 of repetitive energetic proton generation by ultra-intense laser interaction with a tape target. *High Energy*
833 *Density Physics* 37, 100847. doi:10.1016/j.hedp.2020.100847

- 835 Durante, M., Bräuer-Krisch, E., and Hill, M. (2018). Faster and safer? flash ultra-high dose rate in
836 radiotherapy. *The British Journal of Radiology* 91, 20170628. doi:10.1259/bjr.20170628. PMID:
837 29172684
- 838 Favaudon, V., Caplier, L., Monceau, V., Pouzoulet, F., Sayarath, M., Fouillade, C., et al. (2014). Ultrahigh
839 dose-rate flash irradiation increases the differential response between normal and tumor tissue in mice.
840 *Science Translational Medicine* 6, 245ra93–245ra93. doi:10.1126/scitranslmed.3008973
- 841 Fiorini, F., Kirby, D., Borghesi, M., Doria, D., Jeynes, J. C., Kakolee, K. F., et al. (2011). Dosimetry and
842 spectral analysis of a radiobiological experiment using laser-driven proton beams. *Phys Med Biol* 56,
843 6969–6982
- 844 Fitzmaurice, C., Akinyemiju, T. F., Al Lami, F. H., Alam, T., Alizadeh-Navaei, R., Allen, C., et al. (2018).
845 Global, Regional, and National Cancer Incidence, Mortality, Years of Life Lost, Years Lived With
846 Disability, and Disability-Adjusted Life-Years for 29 Cancer Groups, 1990 to 2016. *JAMA Oncology* 4,
847 1553. doi:10.1001/jamaoncol.2018.2706
- 848 Fourkal, E., Li, J. S., Ding, M., Tajima, T., and Ma, C. M. (2003). Particle selection for laser-accelerated
849 proton therapy feasibility study. *Medical Physics* 30, 1660–1670. doi:10.1118/1.1586268
- 850 Fourrier, J., Martinache, F., Meot, F., and Pasternak, J. (2008). Spiral ffag lattice design tools. application
851 to 6-d tracking in a proton-therapy class lattice. *Nucl. Instrum. Meth.* A589, 133–142. doi:10.1016/j.j.
852 nima.2008.01.082
- 853 Gabor, D. (1947). A Space-Charge Lens for the Focusing of Ion Beams. *Nature* 160, 89–90. doi:10.1038/
854 160089b0
- 855 Gauthier, M., Curry, C. B., Göde, S., Brack, F.-E., Kim, J. B., MacDonald, M. J., et al. (2017). High
856 repetition rate, multi-mev proton source from cryogenic hydrogen jets. *Applied Physics Letters* 111,
857 114102. doi:10.1063/1.4990487
- 858 González, W. and Prezado, Y. (2018). Spatial fractionation of the dose in heavy ions therapy: An
859 optimization study. *Medical Physics* 45, 2620–2627. doi:10.1002/mp.12902
- 860 Grote, H. and Schmidt, F. (2003). MAD-X: An upgrade from MAD8. *Conf. Proc. C* 030512, 3497
- 861 Karger, C. P. and Peschke, P. (2017). RBE and related modeling in carbon-ion therapy. *Physics in Medicine
862 & Biology* 63, 01TR02. doi:10.1088/1361-6560/aa9102
- 863 Kraft, S. D., Richter, C., Zeil, K., Baumann, M., Beyreuther, E., Bock, S., et al. (2010). Dose-dependent
864 biological damage of tumour cells by laser-accelerated proton beams. *New Journal of Physics* 12, 85003.
865 doi:10.1088/1367-2630/12/8/085003
- 866 Krest, D., Laslett, L., Jones, L. W., Symon, K., and Terwilliger, K. (1956). *Fixed field alternating gradient
867 particle accelerators*. Tech. Rep. MURA-109, MURA-DWK-KRS-LJL-LWJ-KMT-3, Midwestern
868 Universities Research Association (MURA)
- 869 Kurup, A. (2019). Diagnostics for LhARA. *Low energy ion beam diagnostics workshop, Imperial College*
- 870 Lagrange, J. B., Appleby, R. B., Garland, J. M., Pasternak, J., and Tygier, S. (2018). Racetrack FFAG
871 muon decay ring for nuSTORM with triplet focusing. *JINST* 13, P09013. doi:10.1088/1748-0221/13/
872 09/P09013
- 873 Loeffler, J. S. and Durante, M. (2013). Charged particle therapy—optimization, challenges and future
874 directions. *Nature Reviews Clinical Oncology* 10, 411–424. doi:10.1038/nrclinonc.2013.79
- 875 Malka, V., Fritzler, S., Lefebvre, E., d’Humières, E., Ferrand, R., Grillon, G., et al. (2004). Practicability of
876 proton therapy using compact laser systems. *Medical Physics* 31, 1587–1592. doi:10.1118/1.1747751
- 877 Malmberg, J. H., Driscoll, C. F., Beck, B., Eggleston, D. L., Fajans, J., Fine, K., et al. (1988). Experiments
878 with pure electron plasmas. *AIP Conference Proceedings* 175, 28–74. doi:10.1063/1.37613

- 879 Manti, L., Perozziello, F. M., Borghesi, M., Candiano, G., Chaudhary, P., Cirrone, G. A., et al. (2017).
880 The radiobiology of laser-driven particle beams: Focus on sub-lethal responses of normal human cells.
881 *Journal of Instrumentation* 12. doi:10.1088/1748-0221/12/03/C03084
- 882 Margarone, D., Cirrone, G. A. P., Cuttore, G., Amico, A., Andò, L., Borghesi, M., et al. (2018).
883 Elimai: A laser–driven ion accelerator for multidisciplinary applications. *Quantum Beam Science* 2.
884 doi:10.3390/qubs2020008
- 885 Margarone, D., Velyhan, A., Dostal, J., Ullschmied, J., Perin, J. P., Chatain, D., et al. (2016). Proton
886 acceleration driven by a nanosecond laser from a cryogenic thin solid-hydrogen ribbon. *Phys. Rev. X* 6,
887 041030. doi:10.1103/PhysRevX.6.041030
- 888 Martínez-Rovira, I., W, G., S, B., and Y, P. (2017). Carbon and oxygen minibeam radiation therapy: An
889 experimental dosimetric evaluation. *Medical physics* 44. doi:10.1002/MP.12383
- 890 Masood, U., Bussmann, M., Cowan, T. E., Enghardt, W., Karsch, L., Kroll, F., et al. (2014). A
891 compact solution for ion beam therapy with laser accelerated protons. *Applied Physics B* 117, 41–52.
892 doi:<https://doi.org/10.1007/s00340-014-5796-z>
- 893 Masood, U., Cowan, T. E., Enghardt, W., Hofmann, K. M., Karsch, L., Kroll, F., et al. (2017). A
894 light-weight compact proton gantry design with a novel dose delivery system for broad-energetic
895 laser-accelerated beams. *Physics in Medicine & Biology* 62, 5531–5555. doi:10.1088/1361-6560/aa7124
- 896 Meusel, O., Droba, M., Glaeser, B., and Schulte, K. (2013). Experimental studies of stable confined electron
897 clouds using Gabor lenses. *Conf. Proc. C* 1206051, 157–160. doi:10.5170/CERN-2013-002.157
- 898 Milluzzo, G. et al. (2017). Laser-accelerated ion beam diagnostics with TOF detectors for the ELIMED
899 beam line. *JINST* 12, C02025. doi:10.1088/1748-0221/12/02/C02025
- 900 Milluzzo, G. et al. (2018). Geant4 simulation of the ELIMED transport and dosimetry beam line for
901 high-energy laser-driven ion beam multidisciplinary applications. *Nucl. Instrum. Meth. A* 909, 298–302.
902 doi:10.1016/j.nima.2018.02.066
- 903 Morrison, J. T., Feister, S., Frische, K. D., Austin, D. R., Ngirmang, G. K., Murphy, N. R., et al. (2018).
904 MeV proton acceleration at kHz repetition rate from ultra-intense laser liquid interaction. *New Journal
905 of Physics* 20, 22001. doi:10.1088/1367-2630/aaa8d1
- 906 Nevay, L. J. et al. (2020). Bdsm: An accelerator tracking code with particle-matter interactions. *Computer
907 Physics Communications*, 107200
- 908 NIST (2017). *NIST Standard Reference Database 124* (National Institute of Standards and Technology).
909 doi:<https://dx.doi.org/10.18434/T4NC7P>
- 910 Noaman-ul Haq, M., Ahmed, H., Sokollik, T., Yu, L., Liu, Z., Yuan, X., et al. (2017). Statistical analysis of
911 laser driven protons using a high-repetition-rate tape drive target system. *Phys. Rev. Accel. Beams* 20,
912 041301. doi:10.1103/PhysRevAccelBeams.20.041301
- 913 Obst, L., Göde, S., Rehwald, M., Brack, F.-E., Branco, J., Bock, S., et al. (2017). Efficient laser-driven
914 proton acceleration from cylindrical and planar cryogenic hydrogen jets. *Scientific Reports* 7, 10248.
915 doi:10.1038/s41598-017-10589-3
- 916 Paganetti, H. (2014). Relative biological effectiveness (RBE) values for proton beam therapy. Variations as
917 a function of biological endpoint, dose, and linear energy transfer. *Phys. Med. Biol.* 59, R419
- 918 Paganetti, H. and van Luijk, P. (2013). Biological considerations when comparing proton therapy with
919 photon therapy. *Seminars in Radiation Oncology* 23, 77 – 87. doi:<https://doi.org/10.1016/j.semradonc.2012.11.002>. Controversies in Proton Therapy
- 920 Passoni, M., Bertagna, L., and Zani, A. (2010). Target normal sheath acceleration: theory, comparison with
921 experiments and future perspectives. *New Journal of Physics* 12, 045012. doi:10.1088/1367-2630/12/4/
922 045012
- 923

- 924 Pipek, J. et al. (2017). Monte Carlo simulation of the ELIMED beamline using Geant4. *JINST* 12, C03027.
925 doi:10.1088/1748-0221/12/03/C03027
- 926 Planche, T., Fourrier, J., Lancelot, J. L., Meot, F., Neuveglise, D., and Pasternak, J. (2009). Design of a
927 prototype gap shaping spiral dipole for a variable energy protontherapy FFAG. *Nucl. Instrum. Meth.*
928 A604, 435–442. doi:10.1016/j.nima.2009.02.026
- 929 Pommarel, L., Vauzour, B., Mégnin-Chanet, F., Bayart, E., Delmas, O., Goudjil, F., et al. (2017). Spectral
930 and spatial shaping of a laser-produced ion beam for radiation-biology experiments. *Physical Review*
931 *Accelerators and Beams* 20, 1–10. doi:10.1103/PhysRevAccelBeams.20.032801
- 932 Pozimski, J. and Aslaninejad, M. (2013). Gabor lenses for capture and energy selection of laser driven ion
933 beams in cancer treatment. *Laser and Particle Beams* 31, 723—733. doi:10.1017/S0263034613000761
- 934 Prezado, Y., Dos Santos, M., Gonzalez, W., Jouvion, G., Guardiola, C., Heinrich, S., et al. (2017a). Transfer
935 of Minibeam Radiation Therapy into a cost-effective equipment for radiobiological studies: a proof of
936 concept. *Scientific Reports* 7, 17295. doi:10.1038/s41598-017-17543-3
- 937 Prezado, Y. and Fois, G. (2013). Proton-minibeam radiation therapy: a proof of concept. *Medical physics*
938 40. doi:10.1111/1.4791648
- 939 Prezado, Y., Jouvion, G., Hardy, D., Patriarca, A., Nauraye, C., Bergs, J., et al. (2017b). Proton minibeam
940 radiation therapy spares normal rat brain: Long-Term Clinical, Radiological and Histopathological
941 Analysis. *Scientific Reports* 7, 14403. doi:10.1038/s41598-017-14786-y
- 942 Prezado, Y., Jouvion, G., Patriarca, A., Nauraye, C., Guardiola, C., Juchaux, M., et al. (2018). Proton
943 minibeam radiation therapy widens the therapeutic index for high-grade gliomas. *Scientific Reports* 8.
944 doi:10.1038/s41598-018-34796-8
- 945 [Dataset] PTCOG (2020). Particle Therapy Co-Operative Group
- 946 Reiser, M. (1989). Comparison of gabor lens, gas focusing, and electrostatic quadrupole focusing for
947 low-energy ion beams. In *Proceedings of the 1989 IEEE Particle Accelerator Conference, . 'Accelerator*
948 *Science and Technology*. 1744–1747 vol.3
- 949 Romano, F., Schillaci, F., Cirrone, G., Cuttone, G., Scuderi, V., Allegra, L., et al. (2016a). The elimed
950 transport and dosimetry beamline for laser-driven ion beams. *Nuclear Instruments and Methods in*
951 *Physics Research Section A: Accelerators, Spectrometers, Detectors and Associated Equipment* 829,
952 153–158. doi:<https://doi.org/10.1016/j.nima.2016.01.064>. 2nd European Advanced Accelerator Concepts
953 Workshop – EAAC 2015
- 954 Romano, F. et al. (2016b). The ELIMED transport and dosimetry beamline for laser-driven ion beams.
955 *Nucl. Instrum. Meth. A* 829, 153–158. doi:10.1016/j.nima.2016.01.064
- 956 Schillaci, F. et al. (2019). Advanced Beam Transport Solutions for ELIMAIA: A User Oriented Laser-
957 Driven Ion Beamlines. In *10th International Particle Accelerator Conference*. TUPTS005. doi:10.
958 18429/JACoW-IPAC2019-TUPTS005
- 959 Snavely, R. A., Key, M. H., Hatchett, S. P., Cowan, T. E., Roth, M., Phillips, T. W., et al. (2000). Intense
960 high-energy proton beams from petawatt-laser irradiation of solids. *Phys. Rev. Lett.* 85, 2945–2948.
961 doi:10.1103/PhysRevLett.85.2945
- 962 Symon, K. R., Kerst, D. W., Jones, L. W., Laslett, L. J., and Terwilliger, K. M. (1956). Fixed-field
963 alternating-gradient particle accelerators. *Phys. Rev.* 103, 1837–1859. doi:10.1103/PhysRev.103.1837
- 964 Tanigaki, M., Mori, Y., Inoue, M., Mishima, K., Shiroya, S., Ishi, Y., et al. (2006). Present status of the
965 ffag accelerators in kurri for ads study. In *EPAC 2006 - Contributions to the Proceedings*
- 966 The LhARA consortium (2020). *The Laser-hybrid Accelerator for Radiobiological Applications*.
967 Tech. Rep. CCAP-TN-01. [https://ccap.hep.ph.ic.ac.uk/trac/raw-attachment/](https://ccap.hep.ph.ic.ac.uk/trac/raw-attachment/wiki/Research/DesignStudy/PreCDR/Review/2020-03-31-LhARA_pre_CDR-d2)
968 [wiki/Research/DesignStudy/PreCDR/Review/2020-03-31-LhARA_pre_CDR-d2](https://ccap.hep.ph.ic.ac.uk/trac/raw-attachment/wiki/Research/DesignStudy/PreCDR/Review/2020-03-31-LhARA_pre_CDR-d2).

- 969 0.pdf
970 [Dataset] The World Health Organisation (2020). Cancer. <https://www.who.int/news-room/fact-sheets/detail/cancer>
971
972 Thompson, R. C. (2015). PENNING TRAPS. In *Trapped Charged Particles* (WORLD SCIENTIFIC (EUROPE)), Advanced Textbooks in Physics. 1–33. doi:doi:10.1142/9781786340139_0001
973
974 Tsoupas, N. et al. (1991). Uniform beam distributions using octupoles. *Proceedings of PAC 1991*, 1695–1697
975
976 Uesugi, T. (2018). Betatron Tune Measurement . *FFA School, Osaka*
977 Urakabe, E. et al. (1999). Beam-profile control using an octupole magnet. *Jpn. J. Appl. Phys.* 38, 6145–6149
978
979 Vitti, E. T. and Parsons, J. L. (2019). The radiobiological effects of proton beam therapy: Impact on dna damage and repair. *Cancers* 11. doi:10.3390/cancers11070946
980
981 Vozenin, M.-C., Hendry, J. H., and Limoli, C. L. (2019). Biological benefits of ultra-high dose rate flash 982 radiotherapy: Sleeping beauty awoken. *Clinical Oncology* 31, 407–415. doi:10.1016/j.clon.2019.04.001
983 Wang, H. (2014). Wavefront measurement techniques used in high power lasers. *High Power Laser Science 984 and Engineering* 2
985 Wiggins, S. M., Boyd, M., Brunetti, E., Butler, N. M. H., Feehan, J. S., Gray, R. J., et al. (2019). Application 986 programmes at the Scottish Centre for the Application of Plasma-based Accelerators (SCAPA). In 987 *Relativistic Plasma Waves and Particle Beams as Coherent and Incoherent Radiation Sources III*, eds. 988 D. A. Jaroszynski and M. Hur. International Society for Optics and Photonics (SPIE), vol. 11036, 93 – 989 103. doi:10.1117/12.2520717
990 Wilkens, J. J. and Oelfke, U. (2004). A phenomenological model for the relative biological effectiveness in 991 therapeutic proton beams. *Physics in Medicine and Biology* 49, 2811–2825. doi:10.1088/0031-9155/49/ 992 13/004
993 Willingale, L., Nagel, S. R., Thomas, A. G. R., Bellei, C., Clarke, R. J., Dangor, A. E., et al. (2009). 994 Characterization of High-Intensity Laser Propagation in the Relativistic Transparent Regime through 995 Measurements of Energetic Proton Beams. *Physical Review Letters* 102, 125002. doi:10.1103/ 996 PhysRevLett.102.125002
997 Wilson, J., Hammond, E. M., Higgins, G. S., and Petersson, K. (2020a). Corrigendum: Ultra-High 998 Dose Rate (FLASH) Radiotherapy: Silver Bullet or Fool’s Gold? *Frontiers in Oncology* 10, 210. 999 doi:10.3389/fonc.2020.00210
1000 Wilson, J. D., Hammond, E. M., Higgins, G. S., and Petersson, K. (2020b). Ultra-high dose rate (flash) 1001 radiotherapy: Silver bullet or fool’s gold? *Frontiers in Oncology* 9, 1563. doi:10.3389/fonc.2019.01563
1002 Yogo, A., Maeda, T., Hori, T., Sakaki, H., Ogura, K., Nishiuchi, M., et al. (2011). Measurement of relative 1003 biological effectiveness of protons in human cancer cells using a laser-driven quasimonoenergetic proton 1004 beamline. *Applied Physics Letters* 98, 053701. doi:10.1063/1.3551623
1005 Yonemura, Y., Arima, H., Ikeda, N., Ishibashi, K., Maehata, K., Noro, T., et al. (2008). Status of center 1006 for accelerator and beam applied science of kyushu university. *EPAC 2008 - Contributions to the 1007 Proceedings*
1008 Zeil, K., Baumann, M., Beyreuther, E., Burris-Mog, T., Cowan, T. E., Enghardt, W., et al. (2013). 1009 Dose-controlled irradiation of cancer cells with laser-accelerated proton pulses. *Applied Physics B* 110, 1010 437–444. doi:10.1007/s00340-012-5275-3
1011 Zlobinskaya, O., Siebenwirth, C., Greubel, C., Hable, V., Hertenberger, R., Humble, N., et al. (2014). 1012 The effects of ultra–high dose rate proton irradiation on growth delay in the treatment of human tumor 1013 xenografts in nude mice. *Radiation Research* 181, 177–183. doi:10.1667/RR13464.1